RESEARCH ARTICLE

Key Points:
- First observations of hot flow anomaly-like events at Mercury's bow shock
- New method for studying magnetic turbulence in kinetically active current sheets
- Comparative analysis of HFA events at different planets

Correspondence to:
V. M. Uritsky,
vadim.uritsky@nasa.gov

Active current sheets and candidate hot flow anomalies upstream of Mercury's bow shock

V. M. Uritsky[1,2], J. A. Slavin[3], S. A. Boardsen[1,4], T. Sundberg[1,5], J. M. Raines[3], D. J. Gershman[3], G. Collinson[1], D. Sibeck[1], G. V. Khazanov[1], B. J. Anderson[6], and H. Korth[6]

[1]NASA Goddard Space Flight Center, Greenbelt, Maryland, USA, [2]Physics Department, Catholic University of America, Washington, District of Columbia, USA, [3]Department for Atmospheric, Oceanic and Space Sciences, University of Michigan, Ann Arbor, Michigan, USA, [4]Goddard Planetary Heliophysics Institute, University of Maryland, Baltimore County, Baltimore, Maryland, USA, [5]Center for Space Physics, Boston University, Boston, Massachusetts, USA, [6]Johns Hopkins University Applied Physics Laboratory, Laurel, Maryland, USA

Abstract Hot flow anomalies (HFAs) represent a subset of solar wind discontinuities interacting with collisionless bow shocks. They are typically formed when the normal component of the motional (convective) electric field points toward the embedded current sheet on at least one of its sides. The core region of an HFA contains hot and highly deflected ion flows and rather low and turbulent magnetic field. In this paper, we report observations of possible HFA-like events at Mercury identified over a course of two planetary years. Using data from the orbital phase of the MESSENGER mission, we identify a representative ensemble of active current sheets magnetically connected to Mercury's bow shock. We show that some of these events exhibit magnetic and particle signatures of HFAs similar to those observed at other planets, and present their key physical characteristics. Our analysis suggests that Mercury's bow shock does not only mediate the flow of supersonic solar wind plasma but also provides conditions for local particle acceleration and heating as predicted by previous numerical simulations. Together with earlier observations of HFA activity at Earth, Venus, Mars, and Saturn, our results confirm that hot flow anomalies could be a common property of planetary bow shocks and show that the characteristic size of these events is controlled by the bow shock standoff distance and/or local solar wind conditions.

1. Introduction

The MErcury Surface, Space ENvironment, GEochemistry, and Ranging (MESSENGER) mission [*Solomon et al.*, 2001] provides a deep insight into the structure and dynamics of various plasma regions surrounding Mercury. The data reveal a rather active plasma environment which is in many respects unique within our solar system. The magnetosphere of Mercury has been intensively studied in the context of tail and magnetopause reconnection, magnetic flux transport, ultralow-frequency (ULF) waves and oscillations, propagating dipolarization fronts, and other phenomena [see, e.g., *Anderson et al.*, 2008; *Slavin et al.*, 2008, 2009a, 2009c; *Boardsen et al.*, 2009; *Slavin et al.*, 2010; *Sundberg et al.*, 2010, 2012]. It has been shown that the local interplanetary medium surrounding the planet exhibits turbulent variability over both magnetohydrodynamic (MHD) and kinetic plasma scales [*Korth et al.*, 2010; *Uritsky et al.*, 2011]. This broadband variability should have a significant impact on the Hermean magnetosphere and its response to the solar wind driver.

The present paper focuses on dynamic discontinuities in the Hermean foreshock associated with kinetically active current sheets exhibiting magnetic signatures of hot flow anomalies (HFAs) [*Schwartz et al.*, 1985; *Thomsen et al.*, 1986]. Using the first 180 days of MESSENGER operation after its orbital insertion, we identify a set of interplanetary current sheets magnetically connected to the bow shock. We investigate the influence of these events on magnetic field variability in the adjacent plasma regions in the form of ULF waves in quasi-parallel shock configurations. In the absence of reliable particle measurements, final classification of the detected current sheets as HFAs is not possible. This uncertainty is likely to be resolved by the upcoming BepiColombo mission [see, e.g., *Milillo et al.*, 2005, and references therein].

The paper is organized as follows. In section 2, we present a concise review of HFA observations in planetary bow shocks and summarize magnetic and kinetic signatures of HFA events. Section 3 describes the methodology of our study. Section 4 reports case studies of several candidate HFA events and several examples of active helio current sheets not interacting with Mercury's bow shock. Section 5 reports statistical properties
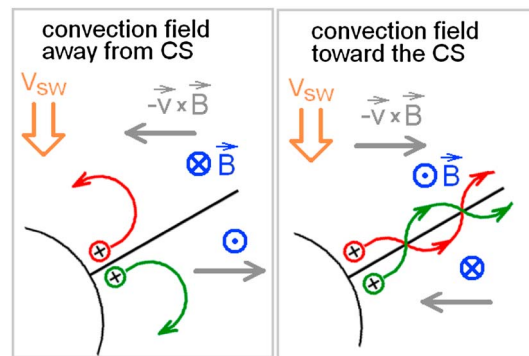
Figure 1. Schematic trajectories of solar wind ions reflected from the bow shock surface into a heliospheric current sheet, with the convection electric field directed away and toward the current sheet. In the former case, the ions gyrate away from the sheet and quickly escape from the contact region; in the latter case, the reflected particles gyrate toward the current sheet and move along it giving rise to a particle beam counterstreaming with the solar wind.

of the observed events including their location, geometry, duration, relative occurrence rates, and other characteristics. Section 6 summarizes the obtained results.

2. Hot Flow Anomalies in Planetary Foreshocks

Collisionless planetary bow shocks do not only mediate the flow of supersonic plasma but also provide conditions for particle acceleration and heating. They can energize, decelerate, and deflect solar wind plasma allowing it to flow through the magnetosheath and around the magnetosphere [*Omidi and Sibeck*, 2007]. For certain shock geometries, the inflowing solar wind plasma can partly return to the upstream region. The interaction between this counterstreaming particle population and the inflowing plasma leads to various plasma instabilities and waves which may effectively energize ions and electrons [*Eastwood et al.*, 2005].

For steady solar wind conditions, the large-scale phenomenology of the foreshock can be organized by the angle $\theta_{B:BS}$ between the upstream magnetic field and the bow shock normal, with the quasi-parallel geometry ($\theta_{B:BS} < 40°$) producing the most extended and dynamic foreshock system populated by backstreaming ions. Changes in the interplanetary magnetic field direction give rise to a variety of small-scale and/or transient foreshock phenomena.

HFAs represent a subset of solar wind discontinuities (rotational or tangential) interacting with the bow shock [*Schwartz et al.*, 1985; *Thomsen et al.*, 1986; *Schwartz et al.*, 2000; *Billingham et al.*, 2011]. They are formed when the normal component of motional electric field points toward the embedded current sheet on at least one of its sides [*Schwartz et al.*, 2000]. The core regions of HFAs typically contain hot and highly deflected ion flows often described by nearly Maxwellian and isotropic particle distributions and rather low and turbulent magnetic fields. The direction of bulk plasma flows in HFAs can differ significantly from that of the ambient solar wind plasma.

The change in the flow velocity in the interior of HFAs relative to the ambient foreshock region is caused by the reflection of solar wind particles from the bow shock. As demonstrated by test particle and hybrid simulations [*Burgess*, 1989; *Thomas et al.*, 1991], the behavior of the reflected ions depends on the motional electric field orientation (see Figure 1). When the convection electric field points away from the sheet, the ions also move away from the current sheet. Once they encounter the bow shock again, they leave the interaction region. In the opposite case, when the convection electric field is directed toward the current sheet, the reflected particles gyrate toward the current sheet on both sides. The returning reflected particles converge on the sheet and results in an ion beam which counterstreams with the ambient solar wind plasma. This process leads to a formation of HFAs if several additional conditions are met.

Since the interaction process, channeling the ions along the current sheet, occurs on the gyration scale of the reflected particles, it is essential that the thickness of the current sheet is comparable with this scale: for thicker current sheets, the trapping effect can be too weak to create a deflected particle flow. In addition, the speed of the transit of the HFA-bow shock intersection must be sufficiently low for the ions to be channeled along the shock [*Schwartz et al.*, 2000]. Global electromagnetic hybrid simulations show that HFAs are only formed during the interaction of a solar wind discontinuity with the quasi-parallel side of the bow shock [*Omidi and Sibeck*, 2007]. The absence of HFAs on the perpendicular side is due to the inability of the reflected ions to escape into the solar wind, as is required by the gyrokinetic mechanism described above.

A prolonged interaction with a quasi-parallel bow shock leads to the development of a flux of suprathermal ions within the core region of HFA events [*Schwartz et al.*, 2006]. The energy of the relative streaming of the reflected particle beam with the ambient solar wind flow is converted into thermal energy in various ways; see, e.g., *Zhang et al.* [2010] and references therein.

The heated plasma expands against the surrounding medium, leading to a low density and magnetic field strength core with compressed regions on both sides of the cavity [*Thomsen et al.*, 1988; *Zhang et al.*, 2010]. Outside the hot core region there are compressed plasma regions consisting of shocked solar wind plasma driven by the expansion of the heated plasma.

The hot central region of fully developed HFAs typically shows isotropic, near-Maxwellian velocity distributions for both ions and electrons. The thermalized interiors of the HFAs are likely to be due to the beam instability [*Tjulin et al.*, 2008] and indicate a strong coupling between various ion components, which is still not quite understood. Transient stages of HFA thermalization can be accompanied by the electromagnetic right-hand resonant ion beam instabilities and lower hybrid waves which are the likely source of electron heating inside the HFAs [*Zhang et al.*, 2013]. While the electron content of the HFAs is energetically less important, it can carry a critical piece of information about the heating mechanism acting in the core of the current sheet. Recent multispacecraft observations [*Hasegawa et al.*, 2012] suggest the possibility of magnetic reconnection within the magnetosheath part of HFAs. If such reconnection does take place it may play a significant part in the acceleration of HFA electrons.

The central region of an HFA is often quite noisy, with a mixture of intervals of depressed and enhanced B-field indicating a presence of embedded current sheets.

The first observations of HFAs near Earth were reported by *Schwartz et al.* [1985] and *Thomsen et al.* [1986] based on the data from the Active Magnetospheric Particle Tracer Explorers and the International Sun - Earth Explorer missions. Subsequent studies have shown that HFA events, also known as hot diamagnetic cavities [*Thomsen et al.*, 1986], appear systematically in the terrestrial foreshock, with the average occurrence rate of about three events per day [*Schwartz et al.*, 2000]. They typically last for a few minutes and have spatial scales of the order of one Earth's radius. HFAs can generate considerable perturbations of the dynamic pressure in the upstream solar wind [*Sibeck et al.*, 1999; *Eastwood et al.*, 2008] and induce significant magnetospheric response, including displacement of the nominal magnetopause position accompanied by auroral brightening [*Sibeck et al.*, 1999], riddling of peripheral boundary layers [*Savin et al.*, 2012], transient ULF geomagnetic pulsations [*Eastwood et al.*, 2011], and other effects.

HFA activity has also been detected at several other planets. Mars Global Surveyor observed a HFA-like hot diamagnetic cavity upstream of the Martian foreshock [*Øieroset et al.*, 2001]. More recently, HFAs were found at Saturn's bow shock based on Cassini data [*Masters et al.*, 2008b, 2009]. Magnetic signatures of HFA events at Venus were first reported by *Slavin et al.* [2009b] using MESSENGER magnetometer data. The presence of HFAs at Venus was later confirmed by magnetic, electron, and ion observations from Venus Express [*Collinson et al.*, 2012].

No HFA-like events at Mercury have been reported until now, owing to technical limitations of available particle detectors onboard Mariner 10 and MESSENGER preventing unambiguous identification of hot counterstreaming ions. In this study, we attempt to overcome this limitation by conducting an in-depth analysis of magnetic field geometry and turbulence associated with candidate HFA events upstream of the Hermean bow shock. Some of these events show signatures of HFA-like active current sheets similar to those on other planets.

3. Data and Methods

3.1. MESSENGER's Orbit and Data

We investigated the first 180 days of the MESSENGER orbital operations (24 March to 19 September 2011) corresponding to two Mercury years. During this time, MESSENGER followed a highly elliptical orbit (periapsis ~200 km, apoapsis ~15,193 km, inclination 82.5°) enabling observations of a significant part of Mercury's foreshock both in the dawn and dusk sectors.

The magnetic field data were obtained from the MAG magnetometer [*Anderson et al.*, 2007]. The three magnetic field components were measured with a three-axis, ring-core fluxgate detector at a typical sampling period $\Delta t = 50$ ms. MAG data were used to locate interplanetary active current sheets connected with the Hermean bow shock, characterize their dynamics and geometry in terms of previous HFA studies, and identify likely instances of HFA events.

We also used the data from the Fast Imaging Plasma Spectrometer (FIPS) [*Andrews et al.*, 2007] whenever the particle observations were available. The ion plasma instrument FIPS onboard MESSENGER measures
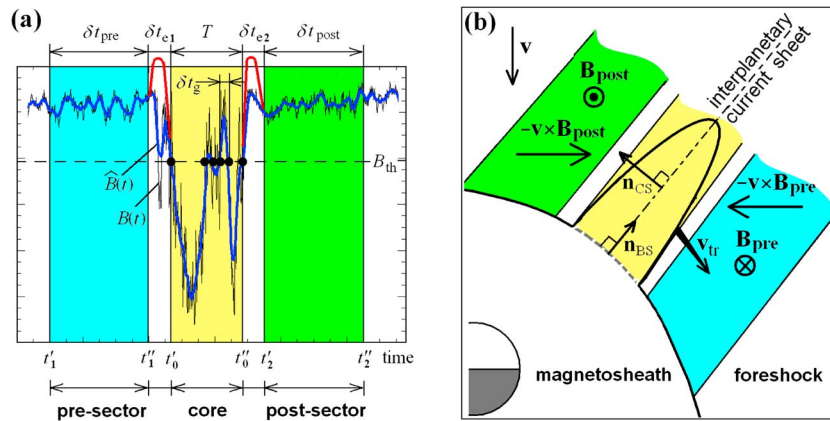
Figure 2. (a) Illustration of the threshold-based detection of an HFA event in the Hermean foreshock. (b) Spatial structure of the event. See text for details.

ions in the energy per charge range of 50 eV/q to 20 keV/q and in the mass per charge range of 1 amu/q to 40 amu/q. The FIPS spectral data used in this study were averaged over the angular field of view of 1.4 Ω, of which 0.4 Ω is obscured by the solar array panels, spacecraft body, and heat shield [*Raines et al.*, 2011], so angular distribution information is not yet available for this data type. The sunshade mounted on the spacecraft body nominally blocks observation of the centroid of the solar wind ion velocity space distributions by FIPS. The most limiting factor in identifying HFA signatures in FIPS observations, however, is the time resolution. The time required for FIPS to complete an energy scan is 64 s or 8 s, depending on the instrument operational mode.

Since the FIPS count rates are a function of plasma drift velocity, temperature, and orientation, these data were interpreted with caution. We used FIPS observations to look for the presence of ions with energies atypical of the expected solar wind, leaving a more rigorous quantitative analysis for future studies.

The Mercury Solar Orbital (MSO) coordinate system is used for all vector quantities, with X_{MSO} directed from the center of the planet toward the Sun, Z_{MSO} being perpendicular to Mercury's orbital plane and pointing toward the north celestial pole, and Y_{MSO} completing the right-handed system.

3.2. Initial Event Detection

The relatively low time resolution and the obscured field of view reduces the ability of FIPS instrument to provide information on transient localized plasma processes near Mercury. In view of this, our event detection was based on MAG data. The core regions of HFAs usually contain intervals of considerable magnetic depression due to the high particle pressure exerted by the hot ions. We used this signature as the starting point of our search for Mercury's HFAs, followed by the analysis of more subtle features including current sheet geometry and detailed B-field variation, reinforced by the analysis of available particle data.

Figure 2 illustrates our event detection criteria and the associated time intervals. The hot core region of the event shown with a yellow rectangle is embedded in a cooler plasma medium which is encountered before and after the event. These encounters are labeled as the presector (blue rectangle) and the postsector (green rectangle), correspondingly. The red magnetic shoulders surrounding the core region are indicative of terrestrial HFA events and are a signature of plasma compression caused by an expansion of the core HFA region. Such magnetic shoulders can be seen in a protoform in some of the Mercury events reported here, although we were unable to find any Mercury events with fully developed compression edges.

The intervals of the depressed magnetic field were identified using the smoothed magnetic field $\widehat{B}$

$$\widehat{B}(t_i) = \frac{1}{w} \sum_{k=i-w/2}^{i+w/2-1} B(t_k) \tag{1}$$

subjected to the threshold condition

$$\widehat{B}(t) < B_{th}, \tag{2}$$

where w is the size of the moving window in time step units. In the presence of fast fluctuations (timescale $\tau \ll w\Delta t$), the smoothed signal $\widehat{B}(t)$ enables more reliable detection of threshold crossings compared to the raw magnetic signal [*Pulkkinen et al.*, 2006a, 2006b]. Low-frequency fluctuations with $\tau \geq w\Delta t$ require additional attention since they can cause $\widehat{B}$ to cross the threshold more than once during the same event. Such fluctuations are commonly observed in the core HFA region where their amplitude can reach the field strength in the surrounding plasma [see, e.g., *Paschmann et al.*, 1988]. To properly attribute multiple B_{th} crossings due to such fluctuations to a single magnetic depression event, we merged together transient magnetic decreases separated by a time gap δt_g of less than 30 s, with the initial smoothing interval of 1 s ($w = 20$).

After a depressed B-field event is detected, we identified three main time intervals corresponding to the observations in the core region of the event ($t \in [t_0', t_0'']$) as well as in its presector ($t \in [t_1', t_1'']$) and the postsector ($t \in [t_2', t_2'']$). The boundaries of the three intervals were calculated as follows (see also Figure 2):

$$t_0' = \min\{t|\widehat{B}(t) < B_{th}\} \tag{3}$$

$$t_0'' = \max\{t|\widehat{B}(t) < B_{th}\} \tag{4}$$

$$t_1' = t_0' - \delta t_{e1} - \delta t_{pre} \tag{5}$$

$$t_1'' = t_0' - \delta t_{e1} \tag{6}$$

$$t_2' = t_0'' + \delta t_{e2} \tag{7}$$

$$t_2'' = t_0'' + \delta t_{e2} + \delta t_{post}. \tag{8}$$

Here B_{th} is the detection threshold, δt_{pre} (δt_{post}) is the duration of the presector (postsector), and δt_{e1} and δt_{e2} are the sizes of the edge regions flanking the core region from either side [*Schwartz*, 1995]. The default values $\delta t_{pre} = \delta t_{post} = 30\,s$ and $\delta t_{e1} = \delta t_{e2} = 10\,s$ were used for the automatic identification of the three regions in the entire set of the detected events. The region boundaries of the events showing clear magnetic signatures of active current sheets were then readjusted by manually taking into account a particular shape of the B-field variation. The locations of the events were evaluated based on the average MSO position of the core region; the event duration T was calculated from the time boundaries of this region:

$$T = t_0'' - t_0'. \tag{9}$$

3.3. Magnetic Geometry

For each magnetic field depression event, we computed the current sheet normal as the cross product between magnetic field before and after the event:

$$\mathbf{n}_{CS} = \pm\mathbf{B}_1 \times \mathbf{B}_2, \tag{10}$$

in which $\mathbf{B}_1$ and $\mathbf{B}_2$ are the average magnetic field vectors in the presector and postsector, correspondingly. The sign ambiguity was resolved by requiring $\mathbf{n}_{CS} \cdot \mathbf{V}_{SW} < 0$, as appropriate for HFA studies [*Schwartz et al.*, 2000]. The solar wind velocity $\mathbf{V}_{SW}$ was assumed to be strictly antisunward and hence parallel to the X_{MSO} axis. We also determined the shortest (projection) distance d_{BS} from the core region of the event to the model bow shock surface describing the average position of Mercury's bow shock for a solar wind fast mode Mach number ~3 [*Slavin et al.*, 2009a]. The same model was used to calculate the local bow shock normal $\mathbf{n}_{BS}$ attached to the projection point.

As stated above, a key HFA formation condition is that the solar wind convection (motional) electric field $\mathbf{E} = -\mathbf{V}_{SW} \times \mathbf{B}$ points into the underlying discontinuity on at least one side (see Figure 2, right). This condition was verified by computing the angles $\theta_{E1:CS}$ and $\theta_{E2:CS}$ between the current sheet normal and the average electric field in the presector and postsector, respectively. We also computed the angle $\theta_{B1:B2}$ between the magnetic vectors $\mathbf{B}_1$ and $\mathbf{B}_2$, the angles $\theta_{B1:BS}$ and $\theta_{B2:BS}$ created by these vectors with the local

bow shock normal $\mathbf{n}_{BS}$, the angle $\theta_{CS:BS}$ between $\mathbf{n}_{CS}$ and $\mathbf{n}_{BS}$, and the angles $\theta_{SW:CS}$ and $\theta_{SW:BS}$ between the solar wind flow direction and each of the two normals.

The magnitude of the magnetic depression events was measured by two parameters—the normalized field jump across the current sheet [*Schwartz et al.*, 2000],

$$\Delta B_{12} = \frac{|B_1 - B_2|}{\max(B_1, B_2)},$$ (11)

and the maximum normalized amplitude of the field decrease in the core region,

$$\Delta B_0 = \frac{B_{12\max} - B_{0\min}}{\max(B_1, B_2)},$$ (12)

in which $B_{12\max}$ is the largest B-field magnitude observed in both presector and postsector and $B_{0\min}$ is the smallest field inside the core region.

To quantify the efficiency of the current sheet-bow shock interaction, we estimated the ratio between the transit velocity of the event, V_{tr}, and the local gyrovelocity of solar wind protons, V_g [*Schwartz et al.*, 1983, 2000]:

$$\left|\frac{V_{tr}}{V_g}\right|_{1,2} = \frac{\cos(\theta_{SW:CS})}{2\cos(\theta_{SW:CS})\sin(\theta_{B1,2:CS})\sin(\theta_{CS:BS})},$$ (13)

where indexes 1 and 2 apply to presector and postsector as usual.

The parameters listed above were used to select candidate HFA events from the automatically detected set of magnetic field depression events satisfying the threshold condition (2). Final selection of the HFA-like events involved manual validation focused on the detailed shape of the magnetic field variation before, during, and after the event, statistical properties of kinetic-scale magnetic field fluctuations indicative of an ion heating, and ion energy spectra.

3.4. Fluctuation Analysis

To investigate statistical properties of magnetic field fluctuations associated with the magnetic depression events, we used the method of higher-order structure function (SF) generalized by *Uritsky et al.* [2011] for the case of strongly nonstationary signals. Using this tool, we compared magnetic turbulence inside and outside the detected events and evaluated the ion crossover scale separating fluid-like and kinetic-like modes of behavior of solar wind plasma [*Schekochihin et al.*, 2007; *Sahraoui et al.*, 2009; *Uritsky et al.*, 2010].

The time-domain higher-order SF is defined as

$$S_q(\tau) = \langle |\delta B_\tau|^q \rangle,$$ (14)

in which δB_τ are the differences of the studied turbulent field B measured at time lag τ, $\langle \cdot \rangle$ denotes averaging over all pairs of points separated by this lag, and q is the order. The SF exponents ζ_q estimated from the scaling ansatz $S_q(\tau) \propto \tau^{\zeta_q}$ provide a detailed description of the turbulent regime under study. The second-order SF $S_2(\tau)$ plays a special role in statistical mechanics of turbulent media as a proxy to the band-integrated wave number Fourier spectrum [*Biskamp*, 2003]. The power law exponent β of the spectrum is related to the SF exponent through $\zeta_2 = \beta - 1$ under the assumption of linear space-time coupling.

Our previous analysis of MESSENGER MAG data using this approach has shown that the Hermean magnetosphere, as well as the surrounding region, are affected by non-MHD effects introduced by finite sizes of cyclotron orbits of the constituting ion species [*Uritsky et al.*, 2011]. Kinetic-scale magnetic fluctuations seem to play a significant role in Mercury's magnetosphere up to the largest resolvable timescale dictated by the signal nonstationarity.

In order to study transient and/or spatially inhomogeneous solar wind fluctuations, we computed local SF estimates made within a sliding window of width W. For each sliding window position, we computed a set of temporal SFs according to equation (14), with $q = 2$ and $\tau < W/2$. The time-dependent shape of the resulting two-dimensional windowed structure function $S_2(\tau, t)$ was represented as a second-order time-period scalogram $\zeta_2(\tau, t)$:

$$\zeta_2(\tau, t) = \frac{\partial \log\left[\frac{1}{W - \tau + 1}\sum_{t'=t-W/2}^{t+W/2-\tau}\left|\widetilde{B}(t') - \widetilde{B}(t' + \tau)\right|^2\right]}{\partial \log \tau}.$$ (15)

Here $\widetilde{B}(t') = B(t') - \phi(t, t', \Delta)$ is the locally detrended magnetic signal, with ϕ being the quadratic polynomial fit to B over the windowed time interval $t' \in [t - W/2, t + W/2]$, τ is the timescale, and t is the running time variable given by the central position of the sliding window. We used quadratic detrending as the simplest way to compensate for the nonstationary trends reflecting spatial inhomogeneity of the traversed plasma structures. Following the approach proposed by *Matthaeus and Goldstein* [1982], the stationarity of the signal was verified based on the ergodic theorem for weakly stationary random processes [*Monin and Yaglom*, 1975]. The partial derivative in the above equation is evaluated from the local least squares linear regression slope of the $S_2(\tau)$ dependence in the log-log coordinates for each sliding window.

The continuous SF scalogram technique defined by equation (15) is essentially different from the widely used wavelet-based or Fourier transform-based dynamic spectrogram techniques [see, e.g., *Alexandrova et al.*, 2006; *Boardsen et al.*, 2009] as it allows analysis of temporal variations of the scaling structure of magnetic fluctuations rather than their spectral amplitudes. As shown in the next section, the SF scalogram provides evidence for drastically different turbulent plasma environments inside and outside the HFA events. In the absence of relevant particle data, this piece of information turns out to be particularly useful.

Using the SF scalogram analysis, we measured the largest temporal scale τ_i at which the power law slope of locally estimated SF is consistent with ion-kinetic ζ_2 values, typically in the range 1.3–1.5 depending on the underlying dispersive wave mode (usually kinetic Alfvén waves or whistler branches with secondary lower hybrid activity) and the turbulence type (i.e., weak or strong); see, e.g., *Yordanova et al.* [2008], *Eastwood et al.* [2009], and *Sahraoui et al.* [2009]. Compressional corrections further increase the kinetic-scale exponents [*Alexandrova et al.*, 2008]. For practical purposes, it is sufficient to use a simplified condition $\zeta_2 \approx 1$ to identify τ_i [*Uritsky et al.*, 2011].

If the Taylor frozen-in flow condition was fulfilled, the ion scale τ_i could be used to evaluate the gyroradius ρ_i and the temperature T_i of the leading ion species [*Uritsky et al.*, 2011]. However, the applicability of the Taylor hypothesis to HFAs is questionable since the bulk flow speed in these regions can be quite small. Under this condition, no accurate inferences about ion distribution temperature or heating can be made about the interiors of candidate HFAs. For this reason, we do not attempt to estimate ion temperature based on the fluctuation analysis and will interpret the timescale τ_i as a stochastic parameter.

4. Case Studies

In this section, we present a subset of magnetic field depression events exhibiting magnetic and kinetic signatures consistent with HFA behavior, as compared to several events associated with passages of helio current sheets (HCSs). All the events were initially detected automatically, after which the boundaries of their presector, postsector, and core sector were adjusted manually to better match their magnetic field profiles not captured by the default definitions. The parameters of the studied HFA-like and non-HFA-like HCSs events are summarized in Tables 1 and 2, correspondingly.

4.1. HFA-Like Events

Ten HFA-like events were identified during the studied 180 day period. Below we provide detailed portraits of four of these events for which FIPS spectra were available.

Event 1 (Figure 3, left) occurred on 16 April 2011 just outside of the bow shock boundary, close to the noon-midnight meridian plane. The event was centered at about 19:00:22 UT and characterized by a normal motional electric field component pointed toward the current sheet in the postsector only ($\theta_{E2:CS} = 151°$). Both leading and trailing edges of the event showed mild magnetic field enhancements, with the trailing edge lasting twice as long compared to the leading edge (respectively, ~3 and ~7 s, or ~1400 and 3200 km at a nominal solar wind speed of 450 km/s). The more pronounced trailing edge may reflect a more favorable E-field orientation on that side [*Thomsen et al.*, 1993]. The described features coexist with an irregular ULF oscillation which precludes their more accurate analysis. The event shows a small B-field rotation angle $\theta_{B1:B2}$ of ~20° and a quasi-parallel magnetic field alignment relative to the local bow shock normal. It is accompanied by a transient reversible change in the $\theta_{B:BS}$ angle. The core region of the event shows significantly reduced B-field magnitude ($\Delta B_0 \sim 1.1$) lasting for about 20 s and a noticeably sharper trailing wall consistent with stronger plasma compression expected on the side exposed to the inwardly directed motional electric field. The normal magnetic field is close to 0, stays fairly constant inside the core region,

Table 1. Parameters of HFA-Like Events

Event	1	2	3	4	5	6	7	8	9	10
mm/dd	04/16	04/16	04/20	04/21	05/04	05/04	05/07	08/13	08/13	08/13
$\frac{(t'_0 + t''_0)}{2}$	19:00:20	19:09:10	04:50:44	03:52:52	06:08:30	18:26:42	04:46:02	04:28:04	04:29:12	02:22:48
X_{MSO}	−0.96	−0.86	1.58	2.20	−0.24	−0.26	−1.29	−3.08	−3.09	−2.13
Y_{MSO}	0.12	−0.01	−1.97	−3.55	−3.78	−3.47	−4.45	−2.42	−2.43	−1.23
Z_{MSO}	−4.50	−4.73	0.42	−1.77	−1.04	−0.58	−3.98	−5.70	−5.69	−6.65
d_{BS}	−0.56	−0.80	−0.50	−2.21	−0.52	−0.19	−1.60	−0.90	−0.88	−1.86
$\theta_{B1:B2}$	18	158	44	81	63	73	2	36	50	32
$\theta_{E1:CS}$	155	37	46	43	52	66	27	74	67	84
$\theta_{E2:CS}$	151	148	108	109	103	152	24	143	142	125
$\theta_{B1:BS}$	159	88	160	136	41	52	69	54	34	40
$\theta_{B2:BS}$	174	94	154	141	22	21	70	25	79	72
$\theta_{CS:BS}$	94	8	90	88	96	96	24	111	112	99
$\theta_{SW:CS}$	112	119	120	130	134	114	98	110	115	123
ΔB_{12}	0.20	0.05	0.41	0.13	0.08	0.09	0.15	0.08	0.15	0.09
ΔB_0	1.09	0.77	2.06	0.48	1.02	1.07	0.62	0.37	0.37	0.28
Δt, s	20	21	18	12	10	6	287	17	13	4
$|V_{tr}/V_g|_1$	0.98	2.87	0.92	0.64	0.86	0.42	0.35	0.48	0.86	0.88
$|V_{tr}/V_g|_2$	3.83	2.88	0.71	0.71	1.46	0.89	0.35	0.90	0.50	0.60

and is 3–5 times lower than the tangential B-field both in the core and in the surrounding plasma environment, an indication of a nearly perpendicular shock [*Paschmann et al.*, 1988]. The jump in the tangential field B_T by a factor of ∼2.5 at the inner wall of the trailing edge implies a jump in the plasma density as required for such shocks.

The core of event 1 shows a very clear and well-localized enhancement of kinetic-scale magnetic turbulence (Figure 3, eighth panel on the left), with the ion-kinetic crossover marked by the yellow color in the chosen color coding rising up to τ_i ∼2 s during the event. The kinetic crossover is not resolved by the MAG

Table 2. Parameters of Non-HFA Events

| Event	11	12	13	14	15	16	17	18	19
mm/dd	04/11	04/13	04/21	04/21	05/06	05/11	07/13	07/27	08/13
$\frac{(t'_0 + t''_0)}{2}$	19:12:18	11:30:20	03:13:34	20:29:00	17:25:30	04:11:09	00:46:29	23:24:28	01:12:30
X_{MSO}	−0.06	3.02	2.30	−0.55	−1.04	−2.20	2.91	−0.67	−1.37
Y_{MSO}	−0.74	−2.74	−3.92	−0.40	−4.41	−3.76	−2.87	0.56	−0.40
Z_{MSO}	−5.66	−5.81	−2.88	−5.49	−2.94	−5.27	−2.08	−5.04	−6.50
d_{BS}	−2.07	−4.54	−2.89	−1.62	−1.18	−1.57	−2.47	−1.20	−2.02
$\theta_{B1:B2}$	116	97	170	108	139	123	141	23	38
$\theta_{E1:CS}$	58	26	68	16	53	69	25	19	85
$\theta_{E2:CS}$	153	141	104	144	114	115	157	20	145
$\theta_{B1:BS}$	131	106	81	139	44	23	57	97	65
$\theta_{B2:BS}$	29	52	93	109	98	100	85	91	100
$\theta_{CS:BS}$	67	39	31	105	67	83	105	17	65
$\theta_{SW:CS}$	115	114	138	106	142	153	112	109	112
ΔB_{12}	0.15	0.13	0.52	0.09	0.15	0.26	0.03	0.10	0.42
ΔB_0	0.48	0.21	0.88	0.70	0.57	0.36	0.98	0.24	0.54
Δt, s	14	31	10	18	18	9	24	3	23
$|V_{tr}/V_g|_1$	0.56	0.50	1.03	0.39	1.12	2.25	0.30	0.99	0.45
$|V_{tr}/V_g|_2$	0.83	0.60	1.02	0.27	0.79	0.92	0.25	0.98	0.42
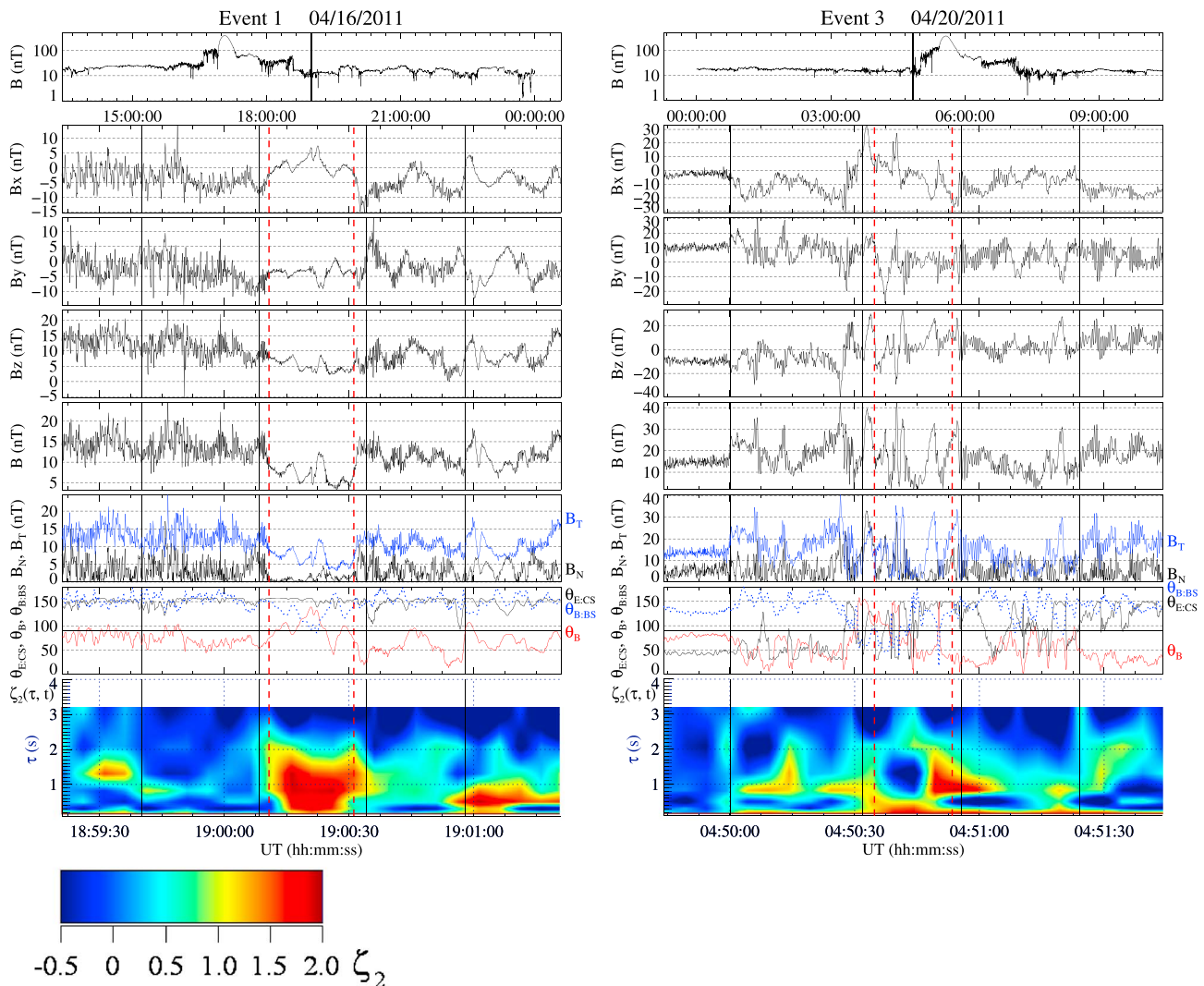
Figure 3. Magnetic and turbulent signatures of two hot flow anomaly events observed on (left) 16 April 2011 and (right) 20 April 2011. (first panel) Large-scale variations of the B-field magnitude B, with the black vertical line marking the timing of the event. Zoomed-in plots of the (second panel) B_x, (third panel) B_y, and (fourth panel) B_z MSO magnetic field components; (fifth panel) the B-field magnitude B; (sixth panel) the tangential (B_T) and normal (B_N) magnetic field components in the current sheet coordinate system determined using equation (10); (seventh panel) the angle $\theta_{E:CS}$ (black line) between the motional E-field and the current sheet normal, the cone angle θ_B (red line) between the magnetic field and the antisunward direction, and the angle $\theta_{B:BS}$ (blue dotted line) between the magnetic field and the bow shock normal; (eighth panel) the SF scalogram showing temporal evolution of the second-order structure function exponent ζ_2 estimated at different temporal scales τ. The ζ_2 color coding is the same for all the scalogram plots presented in this paper. Red dashed vertical lines show the boundaries of the core region, and black solid lines mark the presector and postsector of the event.

instrument in the ambient plasma region, suggesting that τ_i was increased by at least a factor of 10 in the core of this current sheet. The observed change implies a proportional increase of the proton gyroradius which cannot be explained by the much more modest drop of the average field magnitude during the event, unless it was accompanied by a plasma heating.

FIPS spectra show clear particle energization associated with this event. The FIPS spectra were averaged over the instrument's angular field of view. During the presented observation interval, the FIPS E/q range was set to 0.046–13.60 keV/q, and the scan time was 64 s. The color-coded plot in Figure 4 (top) shows the energy versus time spectrogram of the averaged differential proton flux during event 1. There is noticeable increase in the ion energy both preceding and following this active current sheet, with the strongest energization roughly consistent with the position of the core region of the event. Although the low time resolution of FIPS data prevents a more detailed analysis of the structure of this event, it is sufficient for concluding that a hotter ion population may be present. The arrival directions measured by FIPS are consistent with the appearance of a beam-like flow, although the statistics are too limited to be analyzed quantitatively.
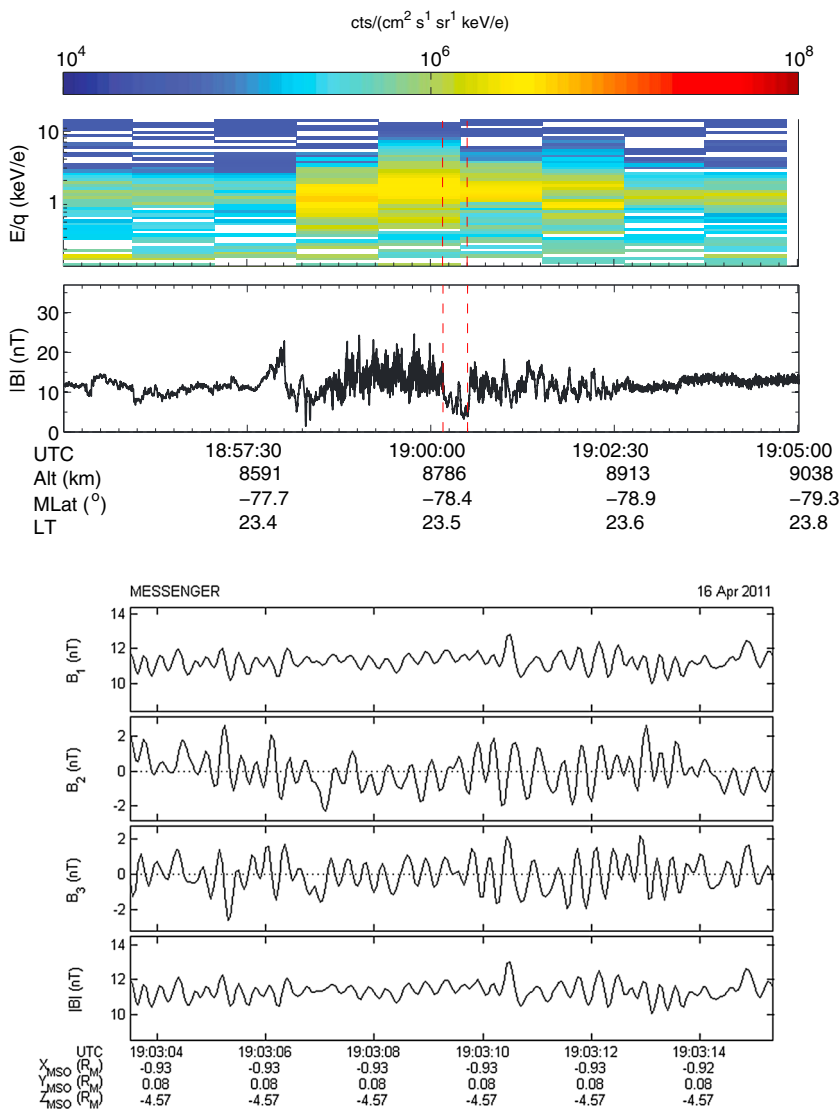
Figure 4. (top) Combined plots of FIPS and MAG observations of the hot flow anomaly event 1 shown in Figure 3 (left). The core region of the event is marked with red vertical lines. (bottom) Left-hand polarized 3–4 Hz wave activity after the event. The right-hand plot is given in field-aligned coordinates, where B_1 is the direction of the mean field over the plotted interval, and B_2 and B_3 are the transverse components, with the corresponding unit vectors $\mathbf{n_1} = [-0.85, 0.51, 0.13]$, $\mathbf{n_2} = [0.52, 0.85, 0.00]$, and $\mathbf{n_3} = [-0.11, 0.066, -0.99]$.

The angle between the motional electric field and the current sheet stayed almost constant in the presector of event 1 (Figure 3, left). It began to show transient departures from the original value of ~150° in the postsector of the event with the motional field being almost parallel to the current sheet plane on several brief occasions. These rotations had an irregular recurrence period of ~7–15 s and could be an indication of unstable plasma conditions which could produce the strong ULF wave oscillations seen a few seconds after the event. These low-frequency waves had a period of ~10 s (0.1 Hz), wave amplitude of ~5–10 nT, a low level of coherence, and a predominant left-hand polarization. A comparison of the minimum variance direction and the field-aligned direction suggests a wave normal angle of ~10–15°. A second high-frequency pulsation, around 3–4 Hz, was present simultaneously. These waves were also left-hand circularly polarized (Figure 4, bottom) and were observed from the edge of the core region until ~19:07 UT. The wave intensity was varying on short timescales and had a behavior similar to that of the electromagnetic ion-cyclotron waves. As the magnetic field in this region is nearly parallel with the bow shock normal, the wave excitation may be driven by backstreaming ions from the bow shock, possibly involving macroscopic current sheet corrugations and instabilities [*Uritsky et al.*, 2001, 2002; *Liu et al.*, 2011; *Liang et al.*, 2010, 2011], along
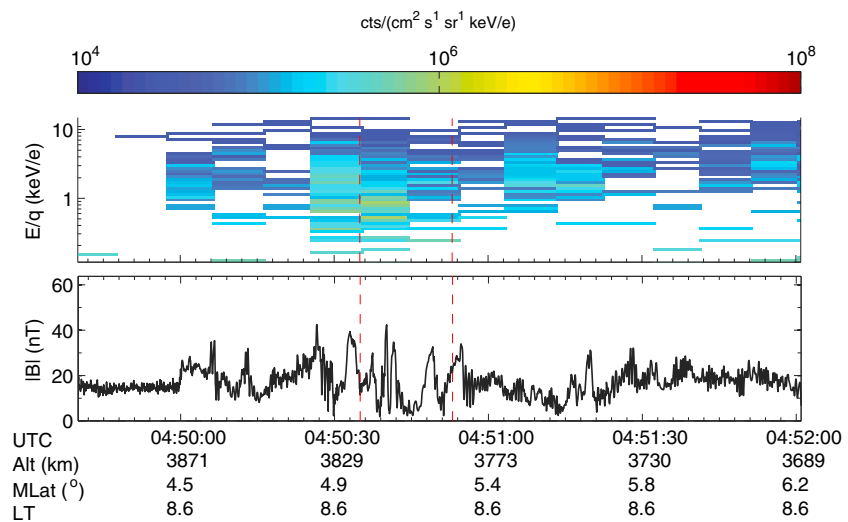
Figure 5. Combined plots of FIPS and MAG observations of the hot flow anomaly event 3 shown in Figure 3 (right). The core region of the event is marked with red vertical lines.

with escaping hot ions from the HFA, which is consistent with the hot ion population observed over the wave interval.

Event 3 (Figure 3, right) was observed at 04:50:30–04:51:00 UT on 20 April 2011. This event had properly oriented motional electric fields pointing toward the current sheet on both sides of the event. The event shows a fairly large difference in the B-field magnitude in the presector and postsector described by $\Delta B_{12} \sim 0.4$ making it an almost certain tangential discontinuity (TD) [*Neugebauer et al.*, 1984]. The magnetic field undergoes several rapid directional changes inside the core region revealing multiple embedded current sheets. A significant normal magnetic field component associated with these changes signals an arbitrary orientation of the small-scale current sheets relative to the main current sheet. The finest temporal scale of the embedded discontinuities is of the order of a tenth of a second which translates into the spatial scale of ~ 40–50 km for typical solar wind conditions. These structures have a kinetic origin and could be supported by several distinct ion populations, deflected at different angles by the bow shock boundary. The intermittent structure of the discussed event resembles short large-amplitude magnetic structures (SLAMS) which are commonly observed at a quasi-parallel terrestrial bow shock [*Schwartz et al.*, 1992] and recently in the foreshock of Venus [*Collinson et al.*, 2012]. The structure of event 3 is similar to SLAMS embedded within a boundary with regions of considerable heating and deceleration. The timescale, polarization parameters, and other characteristics of SLAMS observed at Earth are suggestive of their growth out of ULF wave packets [*Schwartz et al.*, 1992] which are commonly found in HFA cavities. The wavefield of less evolved HFAs can be quite complex [*Tjulin et al.*, 2008]. Event 3 is likely to belong to this category because of its location near the subsolar point suggesting a recent initial interaction with the Hermean bow shock. All other HFA-like events considered in this section were located further downstream and therefore had more time to develop, which may explain their less turbulent core region environment.

The core region of event 3 has well-developed edges with sharp field gradients indicative of strong plasma compression. In the wake of the event, there is a coherent oscillatory activity with a frequency of about 2 Hz which is ~ 10 times higher than the local proton gyrofrequency. The mechanism of this postsector wave activity which we saw in several other Hermean active current sheets remains to be understood. The SF scalogram shows a dramatic increase of the ion crossover scale in the core region of the event, up to ~ 2 s near the inner side of the trailing edge, which may indicate the presence of a local ion heating. The scalogram also suggests that the heated and presumably strongly deflected core particle population "leaks" through the trailing edge into the portion of the postsector adjacent to the event. If this leakage does take place, it can play an important part in the excitation of a plasma instability underlying the 2 Hz wave oscillation in this sector.

During event 3, FIPS operated in its fast scanning mode ensuring an 8 s time resolution. At this sampling time, it is possible to match the heated plasma region with the magnetic signature of the current sheet
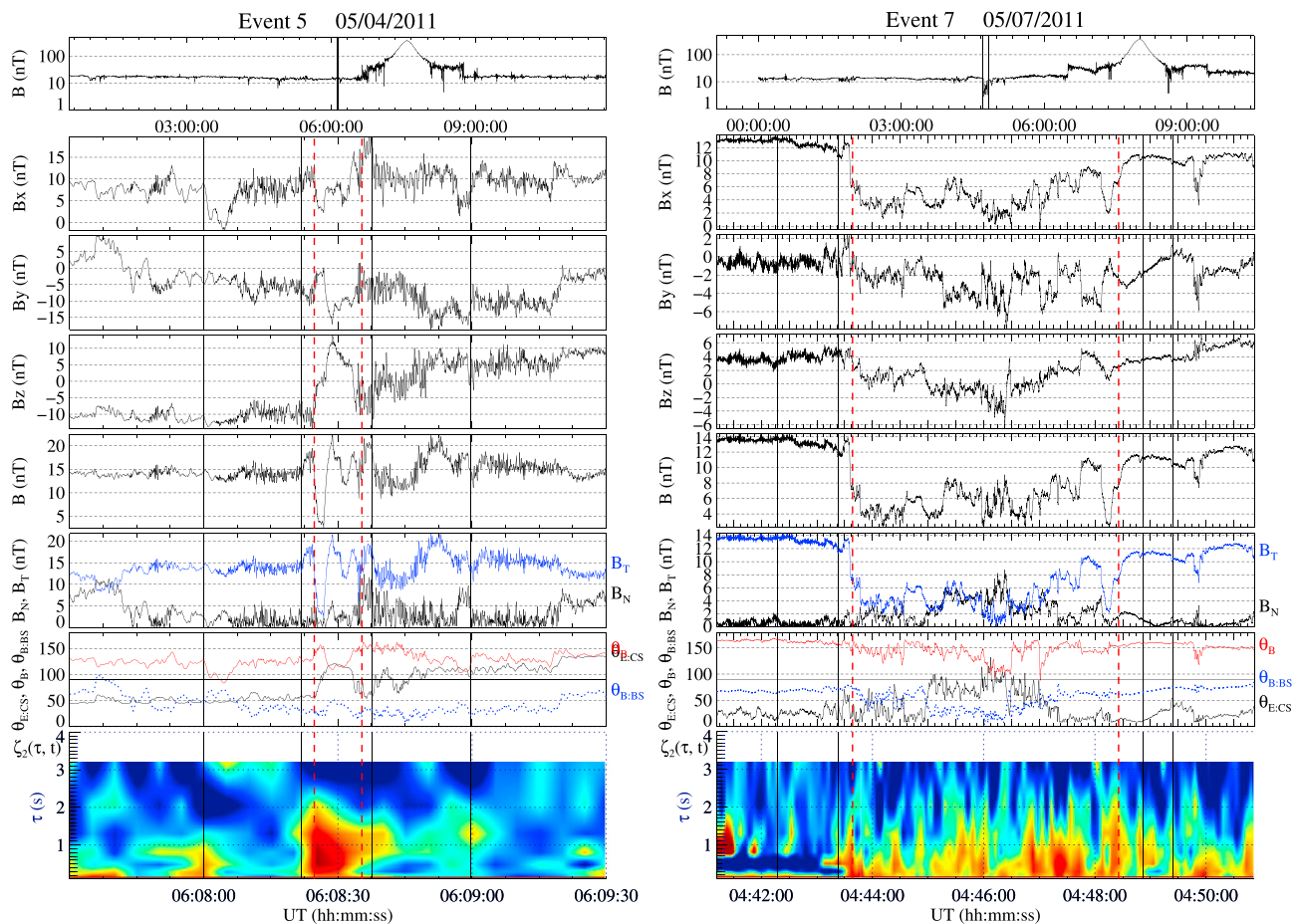
Figure 6. HFA-like events observed on (left) 4 May 2011 and (right) 7 May 2011.

(Figure 5). The presented FIPS spectrogram indicates a substantial plasma heating. In can be seen that the event is associated with a broadened range of energies (∼100 eV to 10 keV) taking place in the core region and at the trailing current sheet.

Event 5 (Figure 6, left) was observed on 4 May 2012 during two subsequent MESSENGER orbits. The event was centered at 06:08:30 UT. Its location is fairly close to the equatorial plane in the dawn foreshock region with a quasi-parallel magnetic field geometry ($\theta_{B:BS}$ ∼20−50°). The event shows classical compression signatures at the leading and trailing edges consistent with the convection E-field pointed inward on either side of the current sheets. It also shows pronounced transient heating signature in the SF scalogram coinciding with the core regions of the events and a significant magnetic field rotation angle of 60–70°.

Event 5 shows a considerable variation of the magnetic field magnitude in the core region characterized by a temporal scale of ∼2 s and an estimated size of ∼900 km. According to the SF scalogram, the core region temperature inside event 5 rises. Overall, event 5 is in a qualitative agreement with the observations of HFAs at Earth's quasi-parallel bow shock.

Event 7 was observed on 7 May 2011 between about 04:43:40 and 04:48:30 (Figure 6, right). It has the longest duration among the detected HFA-like events, with the core region passage lasting for almost 5 min. The "toward" motional electric field is observed in the presector which also features a small but distinct compression edge. The plasma content of the core region is significantly nonuniform. According to the fluctuation scalogram, the leading edge is rather sharp and is associated with a transition from a high-frequency spiky noise (possibly of electrostatic origin [*Singh et al.*, 2007]) outside the event to a cross-scale turbulent cascade observed inside. At the trailing edge, the scaling structure of magnetic fluctuations changes in reverse order, but the time of this transition is not well defined. Irregular variations of the fluid-kinetic
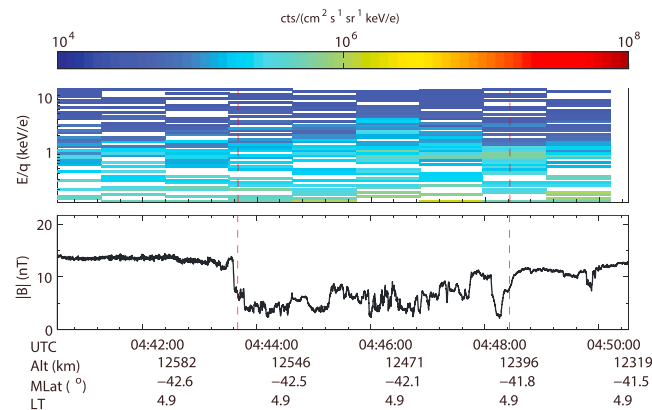
Figure 7. Combined plots of FIPS and MAG observations of the HFA-like event 7 shown in Figure 6 (right column). The core region of the event is marked with red vertical lines.

crossover seen inside the core region confirm the presence of multiple hot plasma layers separated by a substantially cooler plasma. The hottest ion population was likely to be present near the trailing edge where τ_i reaches 1.0–2.0 s suggesting a significant increase in the ion Larmor radius.

Some of the magnetic field depressions inside the core region of event 7 are associated with considerable changes in the magnetic field orientation signaling small-scale current sheets. One such embedded structure was encountered at 04:46:30. It was accompanied by an abrupt 50° change of the θ_B angle. Another rotation for an even larger ~75° angle was detected at about 04:47:00. These compact current-carrying structures can be sites of separate heating events. Some of the local minima in the B-field magnitude are matched by substantial decreases of the normal component hinting at tangential discontinuities. The mutual arrangement of the embedded current sheets does not show stable periodicity and is likely to be shaped by MHD turbulence.

Event 7 is characterized by a weak connection to the bow shock both before and after the core region, with $\theta_{B1:BS} \approx \theta_{B2:BS}$ ~70°, and is located relatively far from the nominal bow shock boundary (d_{BS} ~1.6R_M). The magnetic field rotation between the presector and postsector is unremarkable. Assuming that the hot core region is passively advected with the nominal solar wind speed and taking into account the angle $\theta_{SW:CS}$ between the solar wind flow and the current sheet, the thickness of this HFA is about 7 R_M. The velocity ratio $|V_{tr}/V_g|$ is estimated to be ~0.35 before and after the event, implying that the transit speed was sufficiently slow for the ions to be transported along the shock. The long interaction time could help the development of this event in the quasi-perpendicular bow shock geometry untypical for HFAs.

Ion energization during event 7 is confirmed by FIPS measurements (Figure 7). The most energetic ion population was encountered close to the center of the core region, between 04:46:10 and 04:47:25. The heated plasma extends beyond the trailing event edge into the postsector, in agreement with the washed-out trailing edge position on the SF scalogram as discussed above.

Event 8 was observed on 13 August 2011 (Figure 8), with the core region center at ~04:28:00. It features favorable orientation of the motional E-field at both sides of the current sheet. The postsector shows a somewhat better magnetic connection with the bow shock compared to the presector. The SF scalogram demonstrates a clear-cut fluctuation signature of ion temperature enhancement similar to that seen in other Hermean HFAs. The compression shoulders are missing. Based on this, event 8 could be classified as a proto-HFA event rather than a fully developed HFA.

The FIPS energy spectrogram of event 8 (Figure 9) is much like that of event 3. The spectrogram was obtained in the fast scanning mode and demonstrates a wide range of ion energies ranging from 100 eV to about 2 keV. This behavior is atypical for the solar wind and is consistent with the presence of a local plasma heating. The hotter postsector of event 8 is in an agreement with the asymmetric shape of the turbulence scalogram predicting a larger ion-kinetic scale in that sector compared to the presector.
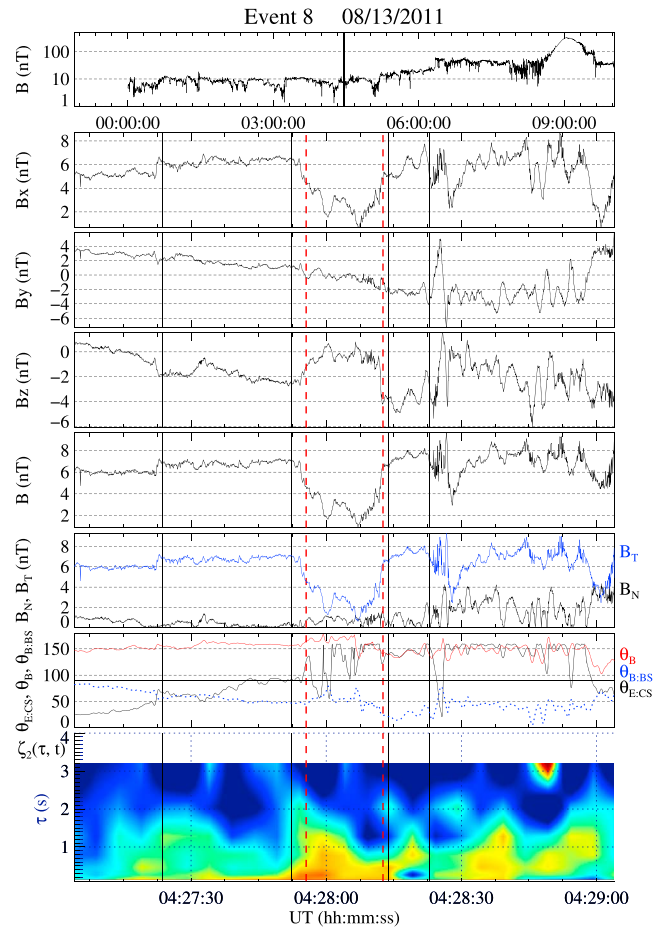
Figure 8. HFA-like event observed on 13 August 2011.

4.2. Non-HFA Active Current Sheets

Our algorithm has detected nine HCS events which show no clear signatures of HFA activity. Table 2 provides a summary of physical and geometric characteristics of these events. These non-HFA current sheets failed to develop HFA signatures by the time of their encounter with MESSENGER despite the proper (toward)
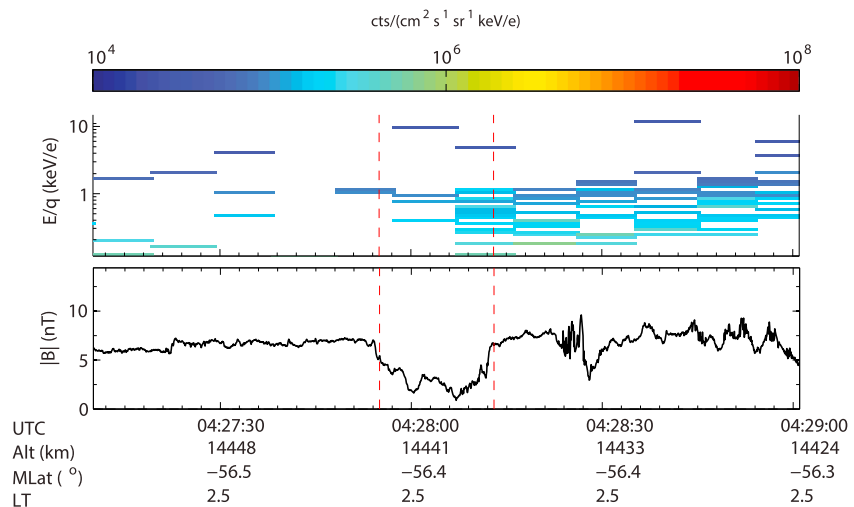

Figure 9. Combined plots of FIPS and MAG observations of the HFA-like event 8 shown in Figure 8. The core region of the event is marked with red vertical lines.

orientation of the presector and postsector convection electric fields and a significant B-field depression in the middle.

The non-HFA events presented in Table 2 have no compressed leading or trailing edges characteristic of HFAs. They feature a large-scale reorganization of the field geometry across the current sheet. The directional E-field change across these current sheets is likely to represent a large-scale solar wind structure rather than a local plasma kinetics and is more indicative of freely propagating helio current sheet than of kinetically active current sheet interacting with the bow shock. All non-HFA helio current sheets were observed at a larger distance from the model bow shock compared to all but one HFAs on our list. The majority of the HCS events featured quasi-perpendicular magnetic field orientation relative to the local bow shock normal. These current sheets were likely to be magnetically disconnected from the bow shock, which prevented their evolution into HFAs.

Compared to HFA-like events, the current sheets presented in this subsection are described by a larger B-field rotation angle accompanied by a smaller relative change of the field magnitude indicative of rotational discontinuities [see *Schwartz et al.*, 2000, and references therein]. The fluctuation signatures of HCS events are also substantially different from those observed for the HFA events. In helio current sheets, the increase of the ion-kinetic crossover at the center of the sheet tends to be less dramatic compared to HFAs and in some HCS events is completely missing. When the ion scale does increase, the enhancement is not well localized.

Events 14 and 15 provide illustrative examples of such delocalized turbulent behavior.

Event 14 detected on 14 April 2011 at ∼20:29:00 (Figure 10, left) reveals the presence of ion-kinetic crossover (at τ_i ∼0.3−0.4 s) both long before and after the current sheet crossing, the type of behavior that HFA events usually do not show. There is a rather short transient increase of the ion scale value to about 1.2 s after which the scalogram returns to its background state. A more consistent increase of τ_i is observed during the passage of the trailing edge of event 14, with the upper range of ion-kinetic scaling reaching 2 s. The blue color-coded gap which is present in the postsector scalogram reveals a distorted shape of the structure function at the intermediate scales. The non–power law scaling associated with this gap could be a manifestation of a strong coherent oscillation inside the core region and the postsector of the event. Polarization parameters of the oscillation are consistent with an obliquely propagating electromagnetic ion-cyclotron wave which could be excited by a two-stream instability caused by reflected solar wind ions.

Event 15 observed on 6 May 2011 at around 17:25:30 (Figure 10, right) demonstrates turbulent signatures of a minor ion heating at the leading edge, according to the shape of the SF scalogram. A similar transient temperature increase took place in the middle of the presector of this HCS event showing that the heating was not limited to the interior of the current sheet. The τ_i enhancement during this event is more evident than that during event 14, but its spatial domain is poorly defined.

Both non-HFA events were associated with long-term changes of angular parameters $\theta_{B:BS}$, $\theta_{E:CS}$, and θ_B showing that these helio current sheets were formed at the interfaces of two large-scale plasma domains with distinct magnetic configurations [*Burlaga et al.*, 1977]. This differs from the HFA-like events considered in the previous section which were characterized by transient changes of the angles emphasizing the localized nature of the observed rotations likely to be associated with heating and deflection of particle beams.

The rest of the HCS events identified by our code (see Table 2) feature similar sets of signatures which are distinct from those accompanying HFA-like events.

5. Statistical Survey

5.1. Event Locations

Figure 11 presents MSO positions of all the detected events classified into several groups. Black dots (n =1337) show automatically detected magnetic depression events satisfying the condition (2) with B_{th}=5 nT. Yellow crosses (n = 100) show filtered events which, in addition to the threshold condition, met a set of criteria making them candidate HFAs. These events had the correct (toward) orientation of the motional electric field on at least one side ($\theta_{E1:CS}$ ∈ [20, 70] and/or $\theta_{E2:CS}$ ∈ [110, 160]), the duration T of the core region between 10 and 100 s, and the distance d_{BS} to the model bow shock lying between −0.5 and
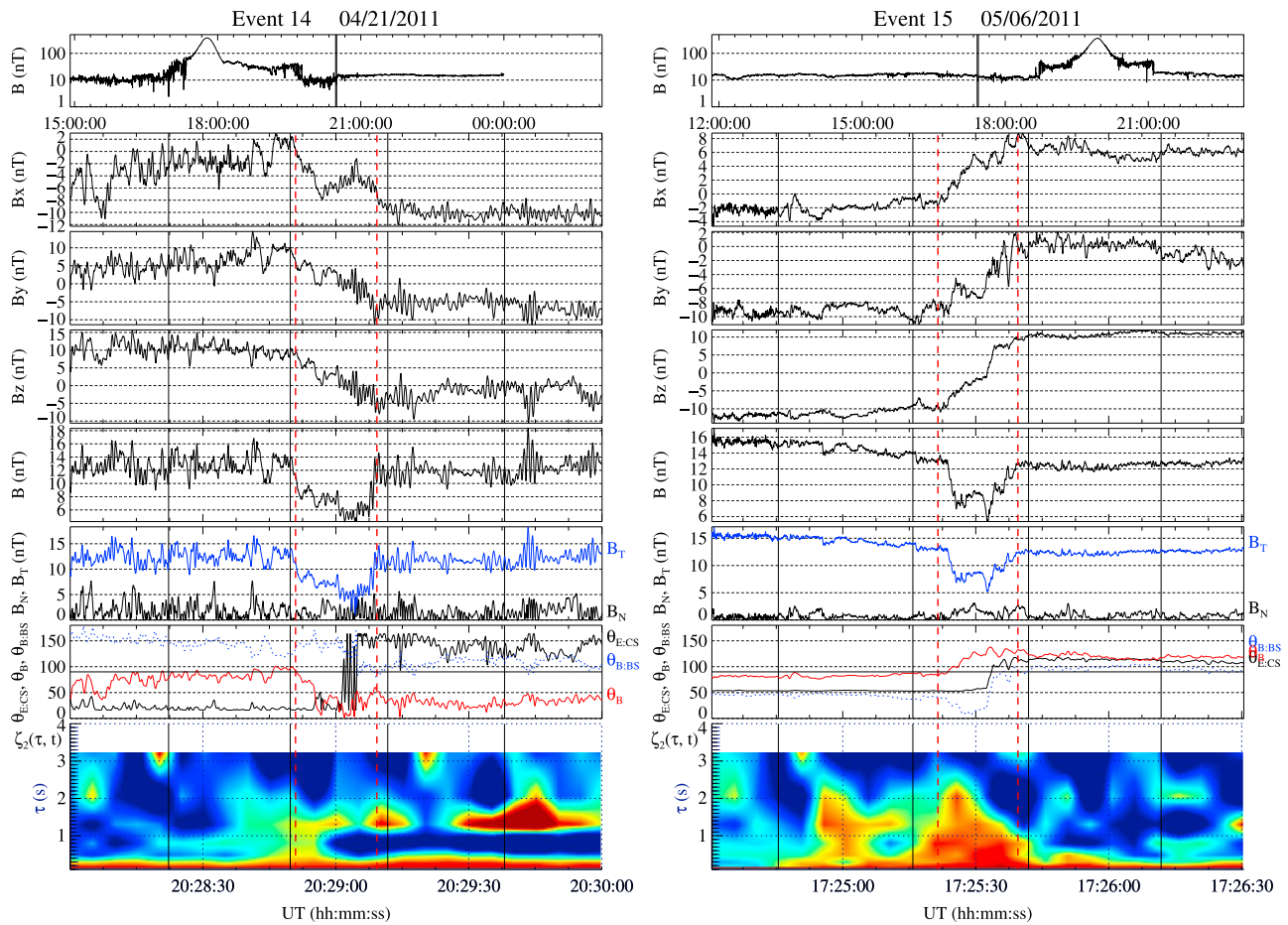
Figure 10. Examples of non-HFA-like heliospheric current sheets in an upstream foreshock region.

3.0 R_M, with the negative (positive) d_{BS} values corresponding to the event positions inside (outside) of the model bow shock boundary.

Red symbols of different pattern designate the subset of the 10 manually selected HFA-like events discussed in detail in the previous section. These events exhibit more reliable magnetic signatures of hot flow anomalies verified using a visual inspection and manual postprocessing. The manually selected events demonstrate identifiable compression edges on one or both sides of the event, a nearly perpendicular mutual orientation of n_{CS} and n_{BS} normals, and a consistently reduced core region B-field ensuring $\Delta B_0 > 0.5$. As discussed earlier in the text, the fluctuation signatures of these events are suggestive of an ongoing ion heating not expected for foreshock cavities.

Blue symbols are used for the set of nine non-HFA HCS events listed in Table 2 which mimic the geometry and large-scale magnetic signatures of the HFAs but lack the compressed edges and turbulent signatures of kinetically active current sheets providing local plasma heating.

The first two planetary years of MESSENGER orbital operation covered a substantial portion of the dawn and dusk portions of the Hermean foreshock. The occurrence probability of all types of detected events is systematically higher in the dawn sector, which is in an agreement with terrestrial studies. It is known that on average, the dawn foreshock has a quasi-parallel magnetic field orientation allowing the reflected ions to be channeled onto the discontinuity. The postmidnight region characterized by large cone angles between the helio current sheets and the antisunward direction is of particular interest as it provides enough time for the kinetic processes to develop [*Schwartz et al.*, 2000]. A similar region at Earth is a preferred location of HFAs and a variety of other intermittent foreshock phenomena [*Tsurutani and Stone*, 1985].
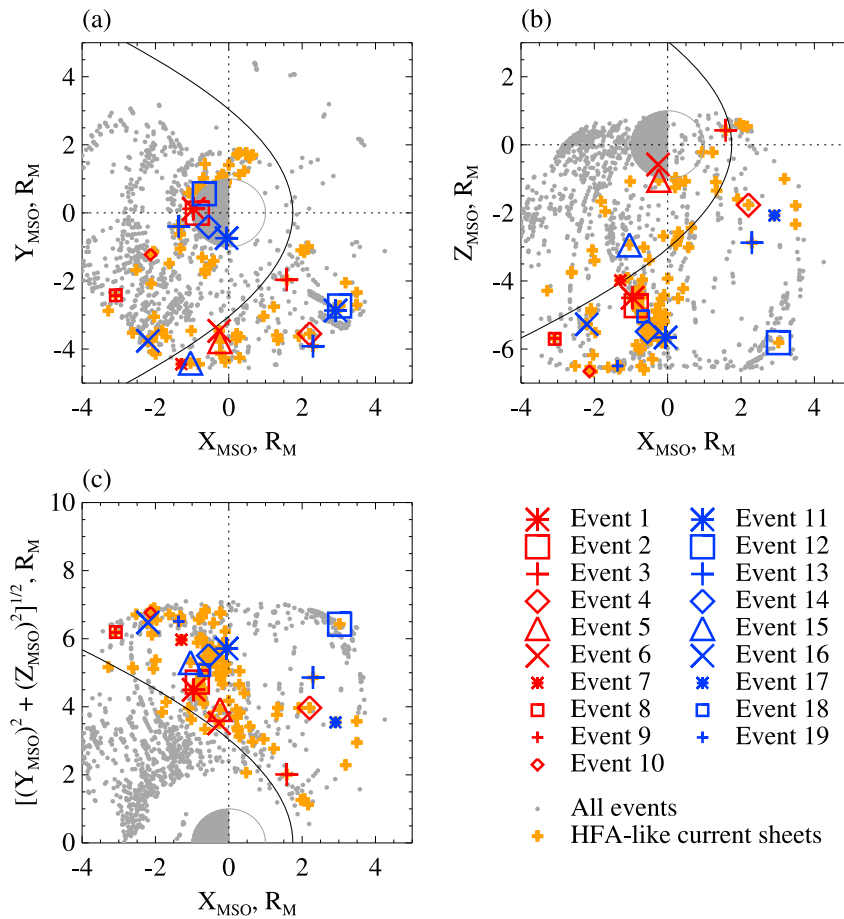
Figure 11. Occurrence locations of the detected events. See text for details.

The automatically detected population of magnetic depression events at Mercury shown by black dots in Figure 11 may include a wide scope of activity not limited to that associated with HFA events, in particular density holes (subminute events sharing many properties of early stage HFAs) [*Parks et al.*, 2006; *Wilber et al.*, 2008], foreshock cavities (transient decreases of magnetic field strength and thermal ion density bounded by HFA-like edges of enhanced B-field) [*Billingham et al.*, 2008], and SLAMS growing out of the ULF wavefield and featuring nonconvective electric fields at the edges [*Schwartz et al.*, 1992]. In its turn, the filtered subset of events (yellow crosses) may, in principle, contain a fraction of HFA or proto-HFA events, although their HFA-like properties cannot be established with certainty. The requirement of the inwardly directed motional electric field on one or both sides removes from our statistics most of the density holes which tend to show an opposite (outward) E-field orientation. The prolonged duration of the filtered events is not characteristic, albeit not impossible, for the SLAMS events observed in the terrestrial foreshock [*Schwartz et al.*, 1992].

As has been already noted, most of the manually validated HFA-like current sheets (except for event 1) are located just outside of the nominal bow shock boundary (Figure 11; see also Table 1), while HCS events are observed systematically farther upstream. At Earth, hot flow anomalies are also formed when an interplanetary discontinuity with convergent motional electric field comes into direct contact with a quasi-parallel bow shock (within ±20% from the model bow shock scaled by the observed solar wind dynamic pressure [*Paschmann et al.*, 1988]). HFA passages are known to induce a magnetosheath response [*Safrankova et al.*, 2000; *Sibeck et al.*, 1999] allowing the magnetopause to move outward ~5 planetary radii beyond its nominal position [*Sibeck et al.*, 1999] and causing significant effects in polar magnetosphere [see, e.g., *Eastwood et al.*, 2011]. Considering the proximity of the events observed here to the bow shock boundary, one can expect that these events play an equally important role in Mercury's magnetosphere.
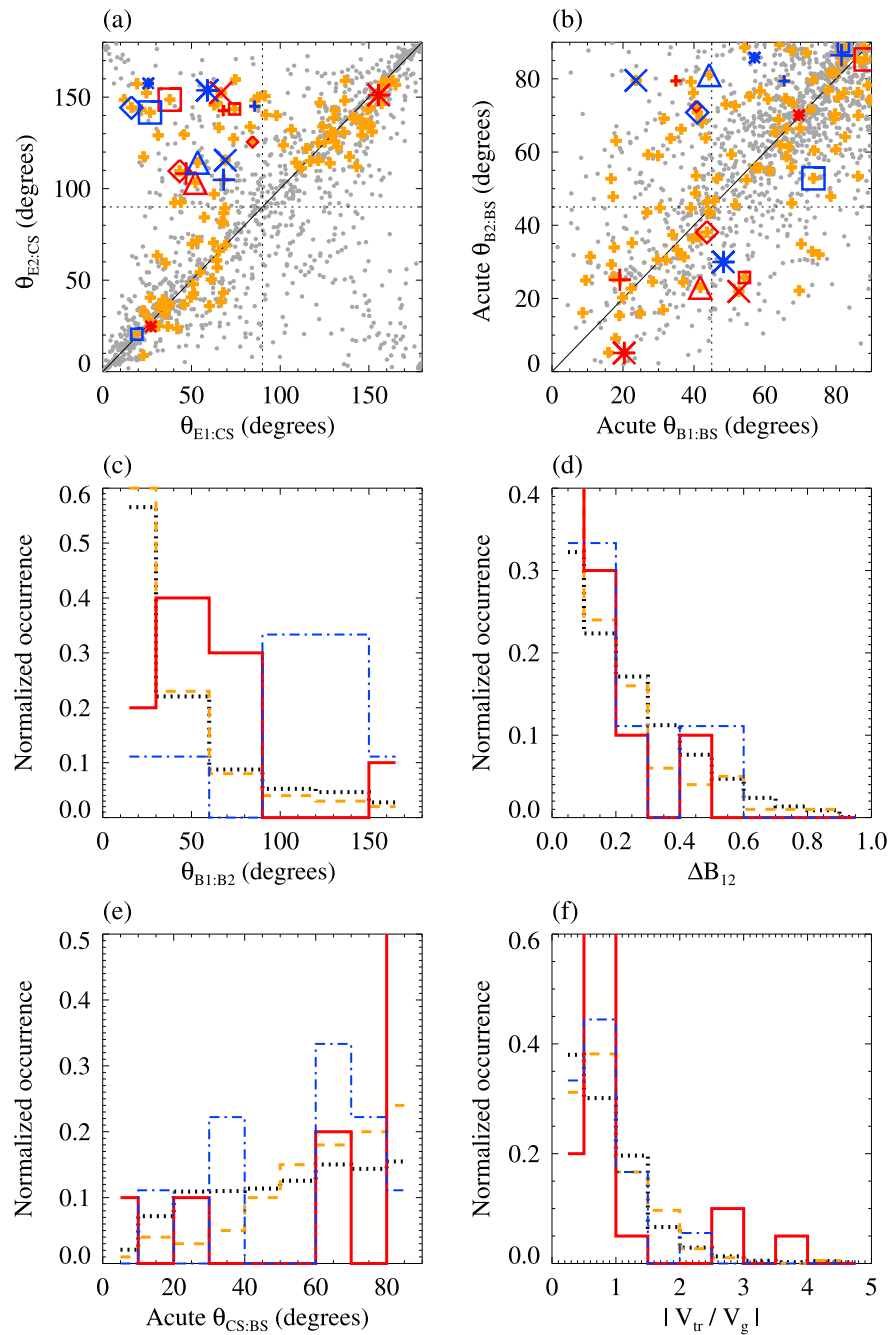
Figure 12. (a–f) Statistical analysis of active current sheets in the Hermean foreshock; see Figure 11 for symbol notations.

5.2. Event Parameters

Figure 12 presents several types of ensemble-based statistics of the detected events.

Figure 12a shows the dependence between the presector and postsector E-field angle with the current sheet normal; Figure 12b demonstrates a similar dependence for the bow shock normal angles with the magnetic field. Figures 12a and 12b use the same symbol notation as in Figure 11.

It can be seen that the majority of the unfiltered magnetic field depression events lie near the diagonal line $\theta_{E1:CS} = \theta_{E2:CS}$ corresponding to a constant motional electric field direction across the current sheet. For $\theta_{E1:CS} < 90°$, the electric field is pointed toward the current sheet in the presector, which causes the solar wind ions that are reflected by the bow shock immediately before the event to gyrate toward the current

sheet. The condition $\theta_{E2:CS} > 90°$ ensures similar behavior of the reflected particles at the trailing edge of the event. When the convection E-field points toward the discontinuity on both sides, the trajectories of the reflected ions from either side converge on the sheet and become channeled along it; see, e.g., *Burgess* [1989] and *Schwartz* [1995]. This configuration leading to the most efficient particle heating corresponds to the upper left corner of the plot. Eight out of 10 events with definite magnetic signatures of HFA-like current sheets are located in this quadrant.

Figure 12b reveals no systematic tendency for the bow shock to become more quasi-perpendicular after the passage of automatically detected active current sheets. This tendency characterizes the behavior of Earth's bow shock before and after HFA events [*Schwartz et al.*, 2000]. Most of the HFA-like events validated manually, especially events 1, 5, 6, and 8, seem to violate this rule making the trailing edge bow shock more quasi-parallel. It remains to be understood whether these exceptions represent a distinct physical environment upstream of Mercury's bow shock or are caused by a statistical uncertainty.

The probability distributions of the angles between the presector and postsector magnetic field shown in Figure 12c demonstrate significant differences. The automatically detected events, filtered and nonfiltered, have a strong peak near $\theta_{B1:B2} \sim 0$ consistent with the fact that motional electric field remains unchanged across most of these events (since $\mathbf{V}_{SW}$ is kept constant). The manually selected HFA events show a systematically stronger B-field rotation peaking at 30–90° which is in a good agreement with the statistics of terrestrial HFAs showing a maximum occurrence rate at 40–90° [*Schwartz et al.*, 2000]. This is also consistent with the scattering of the discontinuity angles describing interplanetary tangential discontinuities found at 0.46 to 0.5 AU [*Lepping and Behannon*, 1986]. The population of HCS events shows an even stronger magnetic rotation with the maximum occurrence rate at 90–150°.

The distribution of the normalized change ΔB_{12} of the field magnitude across the current sheets presented in Figure 12e provides some additional insight into the nature of the underlying interplanetary discontinuities. For a "clean" TD, ΔB_{12} is expected to be greater than 0.2, while smaller values correspond to mixed cases of either rotational or tangential discontinuity, depending on the normal magnetic field component. The ΔB_{12} histogram makes it clear that more than a half of the automatically detected HFA-like events belong to the second (mixed) category. A similar fraction of hot flow anomalies at Earth [*Schwartz et al.*, 2000] have this property. Considering that over 60% of the "mixed" cases may in fact also represent TDs [*Neugebauer et al.*, 1984], the total number of tangential discontinuities in our database should dominate. This is important because our calculations of the current sheet normal is based on the assumption that the current sheets are TDs with a near-zero normal magnetic field component. This assumption is broadly used in single-spacecraft HFA studies. A more accurate identification of $\mathbf{n}_{BS}$ would require a minimum variance analysis through the current sheet which cannot be implemented in the presence of the embedded HFAs.

The probability distribution of $\theta_{CS:BS}$ angles is biased toward large acute angles corresponding to perpendicular orientation of the current sheets relative to the local bow shock. It is similar to the corresponding distribution of terrestrial HFA events (compare with *Schwartz et al.* [2000, Figure 10]). The $\theta_{CS:BS}$ angle needs to be close to 90° in order to keep transit velocity V_{tr} sufficiently small to promote HFA formation. At Earth, about 80% of the HFAs have acute $\theta_{CS:BS}$ angles greater than 60°. Our analysis also yields a significant fraction (~65%) of such events at Mercury. These events had an appropriate spatial orientation with respect to the bow shock which could contribute to their successful development into HFAs. This scenario is supported by the shape of the histogram of the normalized transit velocity $\left|V_{tr}/V_g\right|$ which was constructed by putting together presector and postsector measurements (Figure 12f). The histogram shows a prevailing occurrence rate (above 70%) of smaller-than-one velocity ratios, even though most of the events were observed away from the subsolar point providing optimal current sheet-bow shock intersection conditions. The manually validated HFA-like magnetic depression events have the highest occurrence frequency of smaller-than-unity velocity ratios among the studied groups of events.

5.3. Comparison With Other Planets

It is of interest to compare the estimated sizes of typical and extreme HFA-like events at Mercury with the corresponding sizes of HFA events reported for Earth and Saturn.

To derive characteristic linear sizes of Hermean events, we multiplied the duration of the core region of each event by the nominal solar wind velocity of 450 km/s and applied the correction factor $\cos(\theta_{SW:CS})$
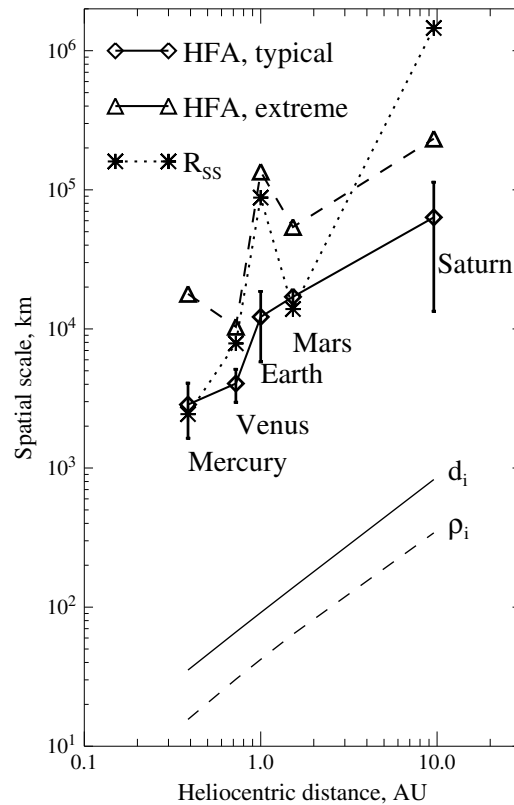
Figure 13. Typical and extreme linear sizes of HFA-like magnetic depression events at Mercury as compared to the sizes of the HFA events at Venus, Earth, Mars, and Saturn, as a function of the heliocentric distance. Overplotted are the average subsolar bow shock standoff distance R_{ss} for each planet and the predicted solar wind ion inertial length d_i and ion gyroradius ρ_i based in the statistical model by *kohnlein* [1996].

accounting for the $\mathbf{n}_{cs}$ misalignment with the solar wind flow. Event 7 whose duration was by an order of magnitude longer than the duration of other events was excluded from the statistics and treated separately.

The typical size of terrestrial HFAs were taken from the global statistical survey conducted by *Facsko et al.* [2009] using their Alfven speed method.

As an example of an extreme terrestrial HFA we choose an event reported by *Safrankova et al.* [2012] based on multispacecraft observations. This event had a rather significant size and caused a considerable magnetosphere deformation.

The typical size of HFA events at Saturn was evaluated using the data reported by *Masters et al.* [2009]; the largest event described in their paper was considered as an extreme event. The Kronian HFA sizes were evaluated for a nominal solar wind velocity of 450 km/s taking into account spatial orientation of the current sheets.

HFA events have been also observed at Venus and Mars. The size of the obstacles introduced by these planets to the solar wind flow is much smaller than that of the Earth's magnetosphere and essentially represents the size of the ionospheres of these planets [*Hasegawa et al.*, 2012]. For the purpose of our comparison, sizes of HFAs at Venus were taken from the studies by *Collinson et al.* [2012, 2013] while Martian HFA event scales were adopted from *Øieroset et al.*

[2001], with the largest HFA sizes found at both planets interpreted as "extreme".

Figure 13 presents the event sizes at the five planets organized by the heliocentric distance. To our knowledge, the cross-planetary HFA comparison shown in this figure is conducted for the first time. Also plotted are characteristic subsolar bow shock standoff distances R_{ss} reported by *Winslow et al.* [2013] (Mercury), *Slavin et al.* [1984] (Venus), *Slavin and Holzer* [1981] and *Russell* [2013] (Earth), *Slavin et al.* [1984] (Mars), and *Masters et al.* [2008a] (Saturn), as well as predicted values of the solar wind ion inertial length d_i and ion gyroradius ρ_i obtained using the empirical model by *kohnlein* [1996].

As can be seen, the size of a typical HFA tends to increase with the size of the planetary bow shock, with the largest (Kronian) events formed at the least curved bow shock boundary. The increase of the ion scales describing an expanding solar wind can contribute to the observed dependence. More research is needed to identify the leading control parameter of the observed dependence.

6. Discussion and Conclusions

We have presented first documented observations of HFA-like magnetic depression events at Mercury. Using magnetic and particle data from MESSENGER collected over a course of two planetary years, we identified a representative ensemble of active current sheets magnetically connected to Mercury's bow shock. Some of these events exhibit magnetic and particle signatures of hot flow anomalies. A broader subset of the detected magnetic depression events is likely to include a variety of plasma disturbances not limited to HFAs, such as the disturbances associated with density holes, foreshock cavities, and SLAMS.

Table 3. Checklist of Key Observational Signatures of HFA Events at Mercury

Signature	Present or Not	Instrument(s)
Presence of interplanetary current sheet	Y	MAG, FIPS
Connection to the bow shock	Y	MAG
Motional electric field orientation enabling particle trapping	Y	MAG
Hot central region	Y	FIPS, MAG
Decrease and/or deflected flow velocity	?	?
Compressed leading or trailing edges	N	MAG
Enhanced low-frequency magnetic fluctuations in the core region	Y	MAG
Size of a few planetary radii	Y	MAG, FIPS
Formation of a bulge on the bow shock surface	?	?

Our classification of current sheets as HFAs is based on an investigation of the current sheet geometry involving all of the commonly used aspects such as the direction of the motional electric field, the bow shock location, the orientation of the current sheet and bow shock normals relative to the solar wind flow, and a number of additional tests. Four of the reported HFA events showed unambiguous signatures of ion energization documented by FIPS dynamic spectra confirming the presence of heated plasma inside and around the current sheets. Although accurate FIPS measurements have limited time resolution and angular coverage, they provided a key piece of evidence by revealing hot plasma populations at the expected locations.

HFA events at Mercury are accompanied by a systematic change in the magnetic turbulence spectrum predicted for a locally energized solar wind plasma. Our previous study [*Uritsky et al.*, 2011] has shown that the Hermean magnetosphere and the surrounding region are affected by non-MHD effects introduced by finite sizes of cyclotron orbits of the constituting ion species. These results have demonstrated that plasma fluctuations at this planet are largely controlled by finite Larmor radius effects. The heating process associated with HFA-like active current sheets explored in the present paper are an important manifestation of such behavior at Mercury.

On one occasion, we detected signatures of a ULF wave packet in a quasi-parallel shock configuration which was likely to be triggered by an HFA event. Such upstream large-amplitude waves may propagate deep into Mercury's magnetosphere causing secondary instabilities in various plasma regions. They can also reach the surface through the thin atmosphere not protected by a conducting ionosphere.

The occurrence rate of HFA-like events at Mercury is systematically higher in the dawn sector compared to the dusk sector. On average, the dawn foreshock has a quasi-parallel magnetic field orientation allowing the reflected ions to be channeled onto the discontinuity. A similar region at Earth is a preferred location of HFAs and a variety of other intermittent foreshock phenomena [*Tsurutani and Stone*, 1985]. The postmidnight region characterized by large cone angles between the helio current sheets and the antisunward direction is of particular interest as it provides enough time for the kinetic processes to develop. Most of our manually validated active current sheets were encountered just outside of the nominal bow shock boundary. Because of their proximity to the bow shock boundary, such events can play an important role in Mercury's magnetosphere. Terrestrial HFAs passages are known to induce a significant magnetosheath response [*Safrankova et al.*, 2000; *Sibeck et al.*, 1999] allowing the magnetopause to move outward ~5 planetary radii beyond its nominal position and perturbing the magnetosphere [see, e.g., *Eastwood et al.*, 2011]. It would be important to verify in future studies whether similar global HFA-induced phenomena occur at Mercury. As an indirect manifestation of such behavior, there is a slight tendency for the bow shock to become more quasi-perpendicular after the passage of HFA-like events, which is also in line with the behavior of Earth's bow shock before and after HFAs [*Schwartz et al.*, 2000].

The characteristic linear size of HFA-like events at Mercury is noticeably smaller than that on other planets. When combined with previously reported HFA sizes at Earth and at Saturn, our measurements show that the size of planetary HFAs grows linearly with planetary radius. The observed dependence could reflect the bow shock geometry. An alternative explanation takes into account the fact that the size of the compared planets is proportional to their distance from the Sun. The increase in the heliocentric distance leads to larger ion scales in the expanding solar wind controlling the thickness of helio current sheets and hence the size of the HFAs.

Schwartz et al. [2000] have provided a concise summary of main observational features of HFA events in the Earth's bow shock which could be used to draw a rigorous conclusion about the nature of similar events at Mercury addressed by our study. These signatures are listed in Table 3 in the context of MESSENGER observations.

It can be seen that many of the essential HFA properties have been positively identified. The HFA-like events studied here occurred within interplanetary current sheets. In each case, there was a time when the current sheet was magnetically connected to the bow shock as evidenced by the time evolution of the $\theta_{B:BS}$ angle. In most cases, motional electric field observed on both sides of this current sheet had a significant "toward" component enabling trapping and acceleration of the reflected ions. FIPS measurements have shown that plasma population in the core of these events tends to be significantly hotter than that in the surrounding regions. This observation is consistent with the increase in the ion crossover frequency in the core regions obtained from the turbulent spectra of magnetic fluctuations. On several occasions, the low-frequency component of magnetic fluctuations was significantly enhanced revealing a rich inner structure of the events. MAG measurements have also confirmed the proximity of the events to the bow shock, with the size of the events comparable with the size of the obstacle as expected.

Some of the HFA signatures have not been observed. Due the obstructed field of view of the plasma spectrometer, it has been impossible to identify the centroid of the velocity distribution function in the core of the events as compared to the ambient solar wind. For this reason, we were unable to verify the presence of a deflected or decelerated plasma flow characteristic of terrestrial HFAs. A single-spacecraft measurement could not provide reliable information on local deformation of the bow shock shape, and so the existence of bow shock bulges caused by HFA events at Mercury remains to be verified. The lack of well-developed leading and trailing edges confirmed by MAG may indicate that the rate of the plasma expansion in the core region was too slow to form noticeable shock waves at the flanks.

In summary, we have demonstrated that Mercury's bow shock contains HFA-like events similar to those observed at other planets. The conducted quantitative analysis suggests that Mercury's bow shock provides conditions for local particle acceleration and heating as predicted by previous numerical simulations. Together with earlier observations of HFA activity at other planets, our results indicate that hot flow anomalies could be a common property of planetary bow shocks. However, since some essential attributes of HFA events have not been found, most importantly the deflected plasma flow and the compressed edges of the core region, it remains to be seen whether the observed events are fully developed HFAs or they should be classified as "proto HFAs" during an early stage of development [*Zhang et al.*, 2010]. The upcoming BepiColombo mission [*Milillo et al.*, 2005] will likely be able to answer this question.

References

Alexandrova, O., A. Mangeney, M. Maksimovic, N. Cornilleau-Wehrlin, J. M. Bosqued, and M. Andre (2006), Alfven vortex filaments observed in magnetosheath downstream of a quasi-perpendicular bow shock, *J. Geophys. Res.*, *111*, A12208, doi:10.1029/2006JA011934.

Alexandrova, O., V. Carbone, P. Veltri, and L. Sorriso-Valvo (2008), Small-scale energy cascade of the solar wind turbulence, *Astrophys. J.*, *674*(2), 1153–1157.

Anderson, B. J., M. H. Acuna, D. A. Lohr, J. Scheifele, A. Raval, H. Korth, and J. A. Slavin (2007), The Magnetometer instrument on MESSENGER, *Space Sci. Rev.*, *131*(1-4), 417–450, doi:10.1007/s11214-007-9246-7.

Anderson, B. J., M. H. Acuna, H. Korth, M. E. Purucker, C. L. Johnson, J. A. Slavin, S. C. Solomon, and R. L. McNutt (2008), The structure of Mercury's magnetic field from MESSENGER's first flyby, *Science*, *321*(5885), 82–85, doi:10.1126/science.1159081.

Andrews, G. B., et al. (2007), The energetic particle and plasma spectrometer instrument on the MESSENGER spacecraft, *Space Sci. Rev.*, *131*(1-4), 523–556, doi:10.1007/s11214-007-9272-5.

Billingham, L., S. J. Schwartz, and D. G. Sibeck (2008), The statistics of foreshock cavities: Results of a Cluster survey, *Ann. Geophys.*, *26*(12), 3653–3667.

Billingham, L., S. J. Schwartz, and M. Wilber (2011), Foreshock cavities and internal foreshock boundaries, *Planet. Space Sci.*, *59*(7), 456–467, doi:10.1016/j.pss.2010.01.012.

Biskamp, D. (2003), *Magnetohydrodynamic Turbulence*, Cambridge Univ. Press, Cambridge, U. K.

Boardsen, S. A., B. J. Anderson, M. H. Acuna, J. A. Slavin, H. Korth, and S. C. Solomon (2009), Narrow-band ultra-low-frequency wave observations by MESSENGER during its January 2008 flyby through Mercury's magnetosphere, *Geophys. Res. Lett.*, *36*, L01104, doi:10.1029/2008GL036034.

Burgess, D. (1989), On the effect of a tangential discontinuity on ions specularly reflected at an oblique shock, *J. Geophys. Res.*, *94*(A1), 472–478, doi:10.1029/JA094iA01p00472.

Burlaga, L. F., J. F. Lemaire, and J. M. Turner (1977), Interplanetary current sheets at 1 AU, *J. Geophys. Res.*, *82*(22), 3191–3200, doi:10.1029/JA082i022p03191.

Collinson, G. A., L. B. Wilson III, D. G. Sibeck, N. Shane, T. L. Zhang, T. E. Moore, A. J. Coates, and S. Barabash (2012), Short large-amplitude magnetic structures (SLAMS) at Venus, *J. Geophys. Res.*, *117*, A10221, doi:10.1029/2012JA017838.

Collinson, G. A., D. G. Sibeck, A. Masters, N. Shane, J. A. Slavin, A. J. Coates, T. L. Zhang, M. Sarantos, S. Boardsen, T. E. Moore, and S. Barabash (2012), Hot flow anomalies at Venus, *J. Geophys. Res.*, *117*, A04204, doi:10.1029/2011JA017277.

Collinson, G. A. (2013), A survey of Hot Flow Anomalies at Venus, *J. Geophys. Res. Space Phys.*, doi:10.1002/2013JA018863, in press.

Eastwood, J. P., E. A. Lucek, C. Mazelle, K. Meziane, Y. Narita, J. Pickett, and R. A. Treumann (2005), The foreshock, *Space Sci. Rev.*, *118*(1-4), 41–94, doi:10.1007/s11214-005-3824-3.

Eastwood, J. P., T. D. Phan, S. D. Bale, and A. Tjulin (2009), Observations of turbulence generated by magnetic reconnection, *Phys. Rev. Lett.*, *102*(3), 035001, doi:10.1103/PhysRevLett.102.035001.

Eastwood, J. P., S. J. Schwartz, T. S. Horbury, C. M. Carr, K. H. Glassmeier, I. Richter, C. Koenders, F. Plaschke, and J. A. Wild (2011), Transient Pc3 wave activity generated by a hot flow anomaly: Cluster, Rosetta, and ground-based observations, *J. Geophys. Res.*, *116*, A08224, doi:10.1029/2011JA016467.

Eastwood, J. P., et al. (2008), THEMIS observations of a hot flow anomaly: Solar wind, magnetosheath, and ground-based measurements, *Geophys. Res. Lett.*, *35*, L17S03, doi:10.1029/2008GL033475.

Facsko, G., Z. Nemeth, G. Erdos, A. Kis, and I. Dandouras (2009), A global study of hot flow anomalies using Cluster multi-spacecraft measurements, *Ann. Geophys.*, *27*(5), 2057–2076.

Hasegawa, H., H. Zhang, Y. Lin, B. U. O. Sonnerup, S. J. Schwartz, B. Lavraud, and Q. G. Zong (2012), Magnetic flux rope formation within a magnetosheath hot flow anomaly, *J. Geophys. Res.*, *117*, A09214, doi:10.1029/2012JA017920.

Kohnlein, W. (1996), Radial dependence of solar wind parameters in the ecliptic, *Sol. Phys.*, *169*(1), 209–213, doi:10.1007/BF00153841.

Korth, H., B. J. Anderson, T. H. Zurbuchen, J. A. Slavin, S. Perri, S. A. Boardsen, D. N. Baker, S. C. Solomon, and R. L. McNutt Jr. (2010), The interplanetary magnetic field environment at Mercury's orbit, *Planet. Space Sci.*, *59*(15), 2075–2085, doi:10.1016/j.pss.2010.10.014.

Lepping, R. P., and K. W. Behannon (1986), Magnetic-field directional discontinuities—Characteristics between 0.46 and 1.0 AU, *J. Geophys. Res.*, *91*(A8), 8725–8741, doi:10.1029/JA091iA08p08725.

Liang, J., B. Ni, E. Spanswick, M. Kubyshkina, E. F. Donovan, V. M. Uritsky, R. M. Thorne, and V. Angelopoulos (2011), Fast earthward flows, electron cyclotron harmonic waves, and diffuse auroras: Conjunctive observations and a synthesized scenario, *J. Geophys. Res.*, *116*, A12220, doi:10.1029/2011JA017094.

Liang, J., V. Uritsky, E. Donovan, B. Ni, E. Spanswick, T. Trondsen, J. Bonnell, A. Roux, U. Auster, and D. Larson (2010), THEMIS observations of electron cyclotron harmonic emissions, ULF waves, and pulsating auroras, *J. Geophys. Res.*, *115*, A10235, doi:10.1029/2009JA015148.

Liu, W. W., L. F. Morales, V. M. Uritsky, and P. Charboneau (2011), Formation and disruption of current filaments in a flow-driven turbulent magnetosphere, *J. Geophys. Res.*, *116*, A03213, doi:10.1029/2010JA016020.

Masters, A., N. Achilleos, M. K. Dougherty, J. A. Slavin, G. B. Hospodarsky, C. S. Arridge, and A. J. Coates (2008a), An empirical model of Saturn's bow shock: Cassini observations of shock location and shape, *J. Geophys. Res.*, *113*, A10210, doi:10.1029/2008JA013276.

Masters, A., C. S. Arridge, M. K. Dougherty, C. Bertucci, L. Billingham, S. J. Schwartz, C. M. Jackman, Z. Bebesi, A. J. Coates, and M. F. Thomsen (2008b), Cassini encounters with hot flow anomaly-like phenomena at Saturn's bow shock, *Geophys. Res. Lett.*, *35*, L02202, doi:10.1029/2007GL032371.

Masters, A., et al. (2009), Hot flow anomalies at Saturn's bow shock, *J. Geophys. Res.*, *114*, A08217, doi:10.1029/2009JA014112.

Matthaeus, W. H., and M. L. Goldstein (1982), Stationarity of magnetohydrodynamic fluctuations in the solar wind, *J. Geophys. Res.*, *87*(NA12), 347–354.

Milillo, A., et al. (2005), Surface-exosphere-magnetosphere system of Mercury, *Space Sci. Rev.*, *117*(3-4), 397–443.

Monin, A. S., and A. M. Yaglom (1975), *Statistical Fluid Mechanics: Mechanics of Turbulence*, vol. 2, MIT Press, Cambridge, Mass.

Neugebauer, M., D. R. Clay, B. E. Goldstein, B. T. Tsurutani, and R. D. Zwickl (1984), A reexamination of rotational and tangential discontinuities in the solar wind, *J. Geophys. Res.*, *89*(NA7), 5395–5408, doi:10.1029/JA089iA07p05395.

Øieroset, M., D. L. Mitchell, T. D. Phan, R. P. Lin, and M. H. Acuna (2001), Hot diamagnetic cavities upstream of the Martian bow shock, *Geophys. Res. Lett.*, *28*(5), 887–890, doi:10.1029/2000GL012289.

Omidi, N., and D. G. Sibeck (2007), Formation of hot flow anomalies and solitary shocks, *J. Geophys. Res.*, *112*, A01203, doi:10.1029/2006JA011663.

Parks, G. K., et al. (2006), Larmor radius size density holes discovered in the solar wind upstream of Earth's bow shock, *Phys. Plasmas*, *13*(5), 050701, doi:10.1063/1.2201056.

Paschmann, G., G. Haerendel, N. Sckopke, E. Mobius, H. Luhr, and C. W. Carlson (1988), Three-dimensional plasma structures with anomalous flow directions near the Earth's bow shock, *J. Geophys. Res.*, *93*(A10), 11,279–11,294, doi:10.1029/JA093iA10p11279.

Pulkkinen, A., A. Klimas, D. Vassiliadis, and V. Uritsky (2006a), Role of stochastic fluctuations in the magnetosphere-ionosphere system: A stochastic model for the AE index variations, *J. Geophys. Res.*, *111*, A10218, doi:10.1029/2006JA011661.

Pulkkinen, A., A. Klimas, D. Vassiliadis, V. Uritsky, and E. Tanskanen (2006b), Spatiotemporal scaling properties of the ground geomagnetic field variations, *J. Geophys. Res.*, *111*, A03305, doi:10.1029/2005JA011294.

Raines, J. M., J. A. Slavin, T. H. Zurbuchen, G. Gloeckler, B. J. Anderson, D. N. Baker, H. Korth, S. M. Krimigis, and R. L. McNutt Jr. (2011), MESSENGER observations of the plasma environment near Mercury, *Planet. Space Sci.*, *59*(15), 2004–2015, doi:10.1016/j.pss.2011.02.004.

Russell, C. T. (2013), Planetary bow shocks, in *Collisionless Shocks in the Heliosphere: Reviews of Current Research*, edited by B. T. Tsurutani and R. G. Stone, pp. 109–130, AGU, Washington, D. C., doi:10.1029/GM035p0109.

Safrankova, J., L. Prech, Z. Nemecek, D. G. Sibeck, and T. Mukai (2000), Magnetosheath response to the interplanetary magnetic field tangential discontinuity, *J. Geophys. Res.*, *105*(A11), 25,113–25,121, doi:10.1029/1999JA000435.

Safrankova, J., O. Goncharov, Z. Nemecek, L. Prech, and D. G. Sibeck (2012), Asymmetric magnetosphere deformation driven by hot flow anomaly(ies), *Geophys. Res. Lett.*, *39*, L15107, doi:10.1029/2012GL052636.

Sahraoui, F., M. L. Goldstein, P. Robert, and Y. V. Khotyaintsev (2009), Evidence of a cascade and dissipation of solar-wind turbulence at the electron gyroscale, *Phys. Rev. Lett.*, *102*(23), 231102, doi:10.1103/PhysRevLett.102.231102.

Savin, S., E. Amata, L. Zelenyi, and V. Lutsenko (2012), Super fast plasma streams as drivers of transient and anomalous magnetospheric dynamics, *Ann. Geophys.*, *30*(1), 1–7, doi:10.5194/angeo-30-1-2012.

Schekochihin, A. A., S. C. Cowley, and W. Dorland (2007), Interplanetary and interstellar plasma turbulence, *Plasma Phys. Controlled Fusion*, *49*(5A), A195–A209, doi:10.1088/0741-3335/49/5A/S16.

Schwartz, S. J. (1995), Hot flow anomalies near the Earth's bow shock, *Adv. Space Res.*, *15*(8-9), 107–116, doi:10.1016/0273-1177(94)00092-F.

Schwartz, S. J., M. F. Thomsen, and J. T. Gosling (1983), Ions upstream of the Earth's bow shock—A theoretical comparison of alternative source populations, *J. Geophys. Res.*, *88*(NA3), 2039–2047, doi:10.1029/JA088iA03p02039.

Schwartz, S. J., D. Burgess, W. P. Wilkinson, R. L. Kessel, M. Dunlop, and H. Luhr (1992), Observations of short large-amplitude magnetic-structures at a quasi-parallel shock, *J. Geophys. Res.*, *97*(A4), 4209–4227, doi:10.1029/91JA02581.

Schwartz, S. J., G. Paschmann, N. Sckopke, T. M. Bauer, M. Dunlop, A. N. Fazakerley, and M. F. Thomsen (2000), Conditions for the formation of hot flow anomalies at Earth's bow shock, *J. Geophys. Res.*, *105*(A6), 12,639–12,650, doi:10.1029/1999JA000320.

Schwartz, S. J., D. Sibeck, M. Wilber, K. Meziane, and T. S. Horbury (2006), Kinetic aspects of foreshock cavities, *Geophys. Res. Lett.*, *33*, L12103, doi:10.1029/2005GL025612.

Schwartz, S. J., et al. (1985), An active current sheet in the solar-wind, *Nature*, *318*(6043), 269–271, doi:10.1038/318269a0.

Sibeck, D. G., et al. (1999), Comprehensive study of the magnetospheric response to a hot flow anomaly, *J. Geophys. Res.*, *104*(A3), 4577–4593, doi:10.1029/1998JA900021.

Singh, N., G. Khazanov, and A. Mukhter (2007), Electrostatic wave generation and transverse ion acceleration by Alfvenic wave components of broadband extremely low frequency turbulence, *J. Geophys. Res.*, *112*, A06210, doi:10.1029/2006JA011933.

Slavin, J. A., and R. E. Holzer (1981), Solar-wind flow about the terrestrial planets. 1—Modeling bow shock position and shape, *J. Geophys. Res.*, *86*(NA13), 1401–1418.

Slavin, J. A., R. E. Holzer, J. R. Spreiter, and S. S. Stahara (1984), Planetary Mach cones—Theory and observation, *J. Geophys. Res.*, *89*(NA5), 2708–2714, doi:10.1029/JA089iA05p02708.

Slavin, J. A., et al. (2008), Mercury's magnetosphere after MESSENGER's first flyby, *Science*, *321*(5885), 85–89.

Slavin, J. A., et al. (2009a), MESSENGER observations of Mercury's magnetosphere during northward IMF, *Geophys. Res. Lett.*, *36*, L02101, doi:10.1029/2008GL036158.

Slavin, J. A., et al. (2009b), MESSENGER and Venus Express observations of the solar wind interaction with Venus, *Geophys. Res. Lett.*, *36*, L09106, doi:10.1029/2009GL037876.

Slavin, J. A., et al. (2009c), MESSENGER observations of magnetic reconnection in Mercury's magnetosphere, *Science*, *324*(5927), 606–610, doi:10.1126/science.1172011.

Slavin, J. A., et al. (2010), MESSENGER observations of large flux transfer events at Mercury, *Geophys. Res. Lett.*, *37*, L02105, doi:10.1029/2009GL041485.

Solomon, S. C., et al. (2001), The MESSENGER mission to Mercury: Scientific objectives and implementation, *Planet. Space Sci.*, *49*(14-15), 1445–1465.

Sundberg, T., S. A. Boardsen, J. A. Slavin, L. G. Blomberg, and H. Korth (2010), The Kelvin-Helmholtz instability at Mercury: An assessment, *Planet. Space Sci.*, *58*(11), 1434–1441, doi:10.1016/j.pss.2010.06.008.

Sundberg, T., et al. (2012), MESSENGER observations of dipolarization events in Mercury's magnetotail, *J. Geophys. Res.*, *117*, A00M03, doi:10.1029/2012JA017756.

Thomas, V. A., D. Winske, M. F. Thomsen, and T. G. Onsager (1991), Hybrid simulation of the formation of a hot flow anomaly, *J. Geophys. Res.*, *96*(A7), 11,625–11,632, doi:10.1029/91JA01092.

Thomsen, M. F., J. T. Gosling, S. A. Fuselier, S. J. Bame, and C. T. Russell (1986), Hot, diamagnetic cavities upstream from the earths bow shock, *J. Geophys. Res.*, *91*(A3), 2961–2973, doi:10.1029/JA091iA03p02961.

Thomsen, M. F., J. T. Gosling, S. J. Bame, K. B. Quest, C. T. Russell, and S. A. Fuselier (1988), On the origin of hot diamagnetic cavities near the Earth's bow shock, *J. Geophys. Res.*, *93*(A10), 11,311–11,325, doi:10.1029/JA093iA10p11311.

Thomsen, M. F., V. A. Thomas, D. Winske, J. T. Gosling, M. H. Farris, and C. T. Russell (1993), Observational test of hot flow anomaly formation by the interaction of a magnetic discontinuity with the bow shock, *J. Geophys. Res.*, *98*(A9), 15,319–15,330, doi:10.1029/93JA00792.

Tjulin, A., E. A. Lucek, and I. Dandouras (2008), Wave activity inside hot flow anomaly cavities, *J. Geophys. Res.*, *113*, A08113, doi:10.1029/2008JA013333.

Tsurutani, B. T., and R. G. Stone (eds.) (1985), *Collisionless Shocks in the Heliosphere: Reviews of Current Research*, Geophysical Monograph, vol. 35, AGU, Washington, D. C.

Uritsky, V. M., A. J. Klimas, J. A. Valdivia, D. Vassiliadis, and D. N. Baker (2001), Stable critical behavior and fast field annihilation in a magnetic field reversal model, *J. Atmos. Sol. Terr. Phys.*, *63*(13), 1425–1433.

Uritsky, V. M., A. J. Klimas, and D. Vassiliadis (2002), Multiscale dynamics and robust critical scaling in a continuum current sheet model, *Phys. Rev. E*, *65*(4), 046113.

Uritsky, V. M., A. Pouquet, D. Rosenberg, P. D. Mininni, and E. F. Donovan (2010), Structures in magnetohydrodynamic turbulence: Detection and scaling, *Phys. Rev. E*, *82*(5), 056326-1–056326-15, doi:10.1103/PhysRevE.82.056326.

Uritsky, V. M., J. A. Slavin, G. V. Khazanov, E. F. Donovan, S. A. Boardsen, B. J. Anderson, and H. Korth (2011), Kinetic-scale magnetic turbulence and finite Larmor radius effects at Mercury, *J. Geophys. Res.*, *116*, A09236, doi:10.1029/2011JA016744.

Wilber, M., G. K. Parks, K. Meziane, N. Lin, E. Lee, C. Mazelle, and A. Harris (2008), Foreshock density holes in the context of known upstream plasma structures, *Ann. Geophys.*, *26*(12), 3741–3755.

Winslow, R. M., B. J. Anderson, C. L. Johnson, J. A. Slavin, H. Korth, M. E. Purucker, D. N. Baker, and S. C. Solomon (2013), Mercury's magnetopause and bow shock from MESSENGER magnetometer observations, *J. Geophys. Res. Space Physics*, *118*, 2213–2227, doi:10.1002/jgra.50237.

Yordanova, E., A. Vaivads, M. Andre, S. C. Buchert, and Z. Vörös (2008), Magnetosheath plasma turbulence and its spatiotemporal evolution as observed by the Cluster spacecraft, *Phys. Rev. Lett.*, *100*(205003), 205003-1 – 205003-4.

Zhang, H., D. G. Sibeck, Q. G. Zong, S. P. Gary, J. P. McFadden, D. Larson, K. H. Glassmeier, and V. Angelopoulos (2010), Time history of events and macroscale interactions during substorms observations of a series of hot flow anomaly events, *J. Geophys. Res.*, *115*, A12235, doi:10.1029/2009JA015180.

Zhang, H., D. G. Sibeck, Q. G. Zong, N. Omidi, D. Turner, and L. B. N. Clausen (2013), Spontaneous hot flow anomalies at quasi-parallel shocks: 1. Observations, *J. Geophys. Res. Space Physics*, *118*, 3357–3363, doi:10.1002/jgra.50376.